Science of the Total Environment 835 (2022) 155516

Contents lists available at ScienceDirect

Science of the Total Environment

journal homepage: www.elsevier.com/locate/scitotenv

Assessing the impact of freshwater discharge on the fluid chemistry in the Svalbard fjords

Ji-Hoon Kim [a,*], Jong-Sik Ryu [b], Wei-Li Hong [c], Kwangchul Jang [d], Young Ji Joo [b], Damien Lemarchand [e], Jin Hur [f], Myong-Ho Park [g], Meilian Chen [h], Moo-Hee Kang [a], Sanghee Park [i], Seung-Il Nam [d], Yun Kyung Lee [f]

[a] Marine Geology & Energy Division, Korea Institute of Geoscience and Mineral Resources, Daejeon 34132, South Korea
[b] Department of Earth and Environmental Sciences, Pukyong National University, Busan 48513, South Korea
[c] Department of Geological Sciences, Stockholm University, Svante Arrhenius Väg 8, SE106-91 Stockholm, Sweden
[d] Division of Glacier Environment Research, Korea Polar Research Institute, Incheon 21990, South Korea
[e] Université de Strasbourg/EOST, CNRS, Institut Terre et Environnement Strasbourg, 5 rue René Descartes, Strasbourg Cedex F-67084, France
[f] Department of Environment & Energy, Sejong University, Seoul 05006, South Korea
[g] CCS Research Center, Kongju National University, 56 Gongjudaehak-ro, Gongju 32588, South Korea
[h] Environmental Program, Guangdong Technion - Israel Institute of Technology, Shantou 515063, China
[i] Divisionof Earth and Environment Sciences, Korea Basic Science Institute, Chungbuk 28119, South Korea

HIGHLIGHTS

- Fluid chemistry in the Svalbard fjords responds to the changing cryosphere.
- Meltwater of the cryosphere and rainfall causes the observed fluid freshening.
- Brine fluid points to the influence of deep-seated submarine permafrost formation.
- Bedrock-fluid interactions modify fluid signatures differently in time and space.
- Cryo-/hydro-/litho-sphere interactions are pivotal to understand regional hydrology.

GRAPHICAL ABSTRACT

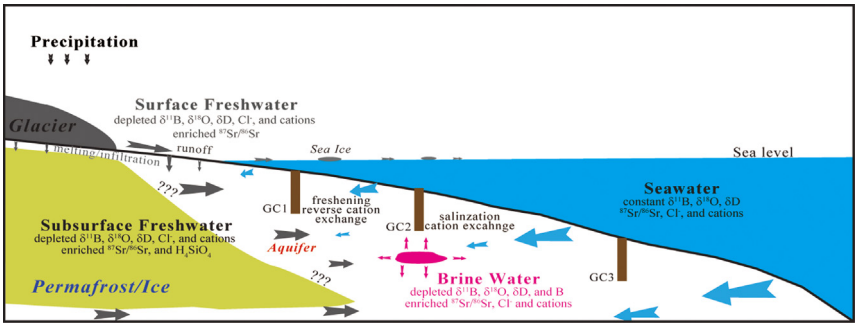

ARTICLE INFO

Editor: José Virgílio Cruz

Keywords:
Freshwater discharge
Brine
Water-rock interactions
Svalbard archipelago
Climate change

ABSTRACT

Changes in the cryosphere extent (e.g., glacier, ice sheet, permafrost, and snow) have been speculated to impact (bio) geochemical interactions and element budgets of seawater and pore fluids in Arctic regions. However, this process has rarely been documented in Arctic fjords, which leads to a poor systematic understanding of land-ocean interactions in such a warming-susceptible region. Here, we present the chemical and isotopic ($\delta^{18}O$, δD, $\delta^{11}B$, and $^{87}Sr/^{86}Sr$) compositions of seawater and pore fluids from five fjords in the Svalbard archipelago. Compared to bottom seawater, the low Cl^- concentrations and depleted water isotopic signatures ($\delta^{18}O$ and δD) of surface seawater and pore fluids delineate freshwater discharge originating from precipitation and/or meltwater of the cryosphere (i.e., glacier, snow, and permafrost). In contrast, the high Cl^- concentrations with light water isotopic values in pore fluids from Dicksonfjorden indicate a brine probably resulted from submarine permafrost formation during the late Holocene, a timing supported by the numerical simulation of dissolved Cl^- concentration.

The freshwater is influenced by the local diagenetic processes such as ion exchanges indicated by $\delta^{11}B$ signatures as well as interactions with bedrock during fluid migration inferred from pore fluid $^{87}Sr/^{86}Sr$ ratios. The interactions with bedrock significantly alter the hydrogeochemical properties of pore fluids in each fjord, yielding spatiotemporal

* Corresponding author.
E-mail address: save@kigam.re.kr (J.-H. Kim).

http://dx.doi.org/10.1016/j.scitotenv.2022.155516
Received 19 February 2022; Received in revised form 11 April 2022; Accepted 21 April 2022
Available online 28 April 2022

variations. Consequently, land-ocean interactions in combination with the hydrosphere-cryosphere-lithosphere are critical factors for understanding and predicting the hydrology and elemental cycling during global climate change periods in the past, present, and future of the Svalbard archipelago.

1. Introduction

The cryosphere in Arctic regions is sensitive to global climate changes through geological time (Peterson et al., 2002; Semiletov et al., 2004; Polyakov et al., 2012), which has immense consequences on the environment and ecosystem. Hydrogeologically, the dynamics of terrestrial ice sheets and permafrost have been proposed to impact the submarine fluid observed in the circum Arctic off Norway, Canada, and Alaska, as well as the Laptev Sea and Greenland Shelf (DeFoor et al., 2011; Lecher et al., 2016; Charkin et al., 2017; Hong et al., 2019; Kim et al., 2021). The same processes also lead to significant perturbations in the marine (bio/geo) chemistry and ecosystems in the Arctic region by delivering trace elements, nutrients, rare earth elements, and dissolved organic matter (Frey and McClelland, 2009; Chen et al., 2016, 2021; Colombo et al., 2018; Kim et al., 2021).

Fluctuations in glacier coverage in the Svalbard archipelago make it one of the key Arctic regions to study the interactions between glacier dynamics and climate changes in the present and on geological time scales. In this region, deglaciation terminated at ~11.2 ka BP (before present) and a warm period lasted until 9 to 8 ka BP, whereas the expansion of glaciers occurred between 6 and 4 ka BP. Most glaciers reached their maximum Holocene extents during the Little Ice Age (LIA) (Svendsen and Mangerud, 1997; Forwick and Vorren, 2009; Baeten et al., 2010; Farnsworth et al., 2020; Jang et al., 2020). The repeated advance and retreat of glaciers throughout the Holocene have led to critical changes in seawater and pore fluid systems in both the land and the ocean (e.g., the formation of straits, creation of islands, hydrology of downstream systems, current circulation, and the permafrost formation and thawing) (Blaszczyk et al., 2013; Grabiec et al., 2018). When conditions allow, large amounts of meteoric freshwater can be produced from the glaciers that transport dissolved solutes to the ocean via surface runoff and/or submarine groundwater discharge (Hagen et al., 2003; Haldorsen et al., 2010; Hong et al., 2019).

The Svalbard archipelago has been impacted by the warming climate. From 1971 to 2017, the annual temperature increased an average of 4.0 °C over the entire archipelago, which is substantially higher than the rise in global average temperature (0.83 °C) for the same period (Hanssen-Bauer et al., 2019). The surging annual temperature together with the more frequent extreme precipitation (Serreze et al., 2016; Vikhamar-Schuler et al., 2016; Peeters et al., 2019) led to a rapid decrease in the glacial surface area by 16% between 1936 and 1990, and a further 7% reduction over the past three decades (Nuth et al., 2007, 2013). By applying the average glacier retreat rate from 2000 to 2015, it has also been predicted that the opening of a strait between Sørkapp Land (south of Hornsund; Fig. 1) and the rest of Spitsbergen Island will likely occur between 2055 and 2065 (Grabiec et al., 2018). Thus, to date, the accelerating shrinkage of the cryosphere extent in the Svalbard archipelago has drawn attention to the potential consequences on the environment and ecosystem from land to ocean, such as hydrology, hydrodynamics, sediment flux, and biota. However, most studies on freshwater discharge in this area have focused on the groundwater from the prominent terrestrial features such as pingos (Yoshikawa and Harada, 1995; Hodson et al., 2019) and springs (Haldorsen and Heim, 1999; Olichwer et al., 2012) with less focus on the impact of groundwater discharge to the marine environment. Although these studies have provided considerable information about how the groundwater system is influenced by cryosphere dynamics, they fail to reveal the regional consequences as fresh groundwater flows into the fjord and marine system around the Svalbard archipelago. As a result, key knowledge of the extent of freshwater discharge from the region is still missing. It is also not clear how offshore groundwater impacts the regional hydrological system, alters the chemical properties of seawater and pore fluids, and interacts with bedrock and/or aquifers under current and past global climate changes.

Here, we report the compositional and isotopic signatures of seawater and pore fluids from five fjords (Isfjorden, Dicksonfjorden, Tempelfjorden, Van Mijenfjorden, and Hornsund fjord) in the Svalbard archipelago (Fig. 1). We observe fluid freshening in both surface seawater and pore fluid while brine fluid is found only in pore fluid, reflecting the cryosphere fluctuation in each fjord in response to climate changes. We also identify geochemical signatures that suggest fluid-bedrock interactions. Ultimately, we elucidate the origin and alteration of seawater and pore fluid in the Svalbard archipelago. Numerical modeling of the dissolved chloride profiles reveals a response time of several centuries with an ascending freshwater front in the fjord sediments. Such a result suggests that the hydrosphere-cryosphere-lithosphere connection has likely been occurring in the Svalbard archipelago since the late Holocene. Our findings contribute to a more comprehensive understanding and a better prediction of the impact of the increasing meltwater discharge of the cryosphere on the seawater and pore fluid chemistry in the Arctic coastal regions, in response to future global climate changes.

2. Regional setting

The Svalbard archipelago is located in the northwestern Barents Sea between 74° N and 81° N with a total land area of 63,000 km^2. Approximately 60% of the land area is covered by glaciers, corresponding to ~10% of the Arctic glacier area, excluding the Greenland ice sheet (Onarheim et al., 2014). Since the archipelago lies between the Fram Strait and the Barents Sea at the outer reaches of the warm North Atlantic Current (Loeng, 1991; Nuth et al., 2010), it experiences a relatively warm and variable climate compared to other regions at similar latitudes.

We investigated five different fjords along the main island of the archipelago, Spitsbergen; Isfjorden, Dicksonfjorden, Tempelfjorden, Van Mijenfjorden, and Hornsund fjord (Fig. 1). Isfjorden, the largest fjord system in the Svalbard archipelago (ca. 100 km long and up to 425 m deep), is dominated by partly deformed sedimentary rocks of Devonian to Neogene age, with deformed Proterozoic metamorphic rocks occurring in the western part of the fjord. Unconsolidated Quaternary fluvial and marine deposits appear in valleys and on raised strand flats (Dallmann, 2015). The inner parts of Isfjorden were deglaciated approximately 10 ka BP, suggesting that it probably had not been influenced by tidewater glaciers during the early- (11.7–8.2 ka BP) and mid-Holocene (8.2–4.2 ka BP) (Svendsen and Mangerud, 1997). The major readvances of the glaciers commenced during the late Holocene (4.2 ka BP to the present), culminating in maximum glacier extents at different times (Werner, 1993; Svendsen et al., 1996; Svendsen and Mangerud, 1997; Farnsworth et al., 2020).

Dicksonfjorden and Tempelfjorden are the tributary fjords of the Isfjorden system. Dicksonfjorden is a north-south oriented fjord that is approximately ~30 km long and ~7 km wide (Hagen et al., 1993). Devonian fluvial siltstones and sandstones are the predominant bedrock in the area and Carboniferous-Permian mixed carbonate-siliciclastic strata are partly observed (Dallmann, 2015). Tempelfjorden is ~14 km long and up to 5 km wide and comprises a sinuous-shaped basin with a maximum water depth of 110 m in the central and outer parts of the fjord. A smaller glacier-proximal basin with a water depth reaching 70 m is located in the inner fjord (Plassen et al., 2004). Carboniferous and Permian carbonates as well as evaporites with subordinate silicified carbonates and clastic strata comprise the bedrock in the area (Dallmann, 2015).

Van Mijenfjorden is ~50 km long and 10 km wide and contains two main basins separated by a sill. The innermost basin reaches a depth of ~50–60 m, whereas the outer, larger basin is approximately twice as

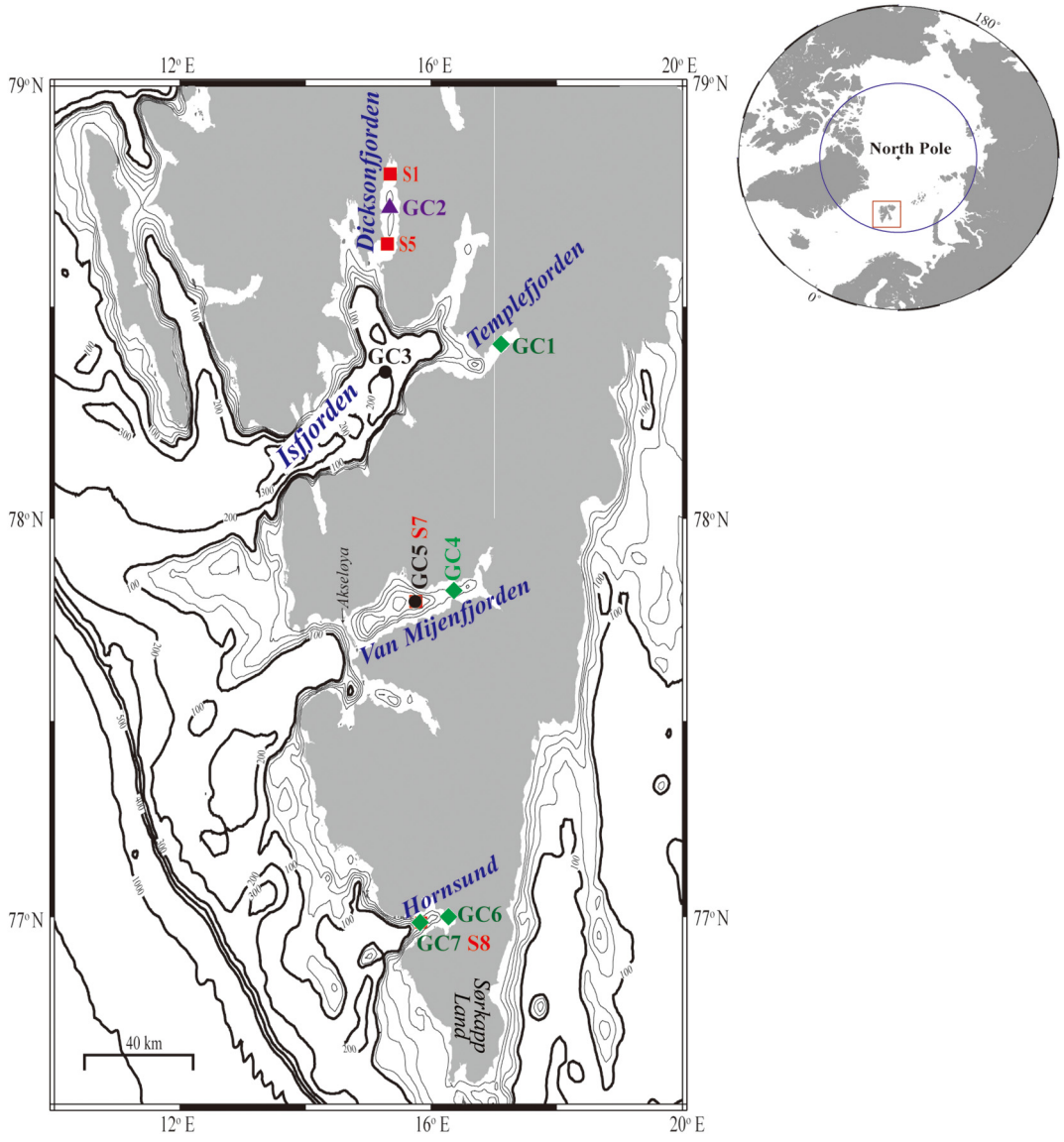

Fig. 1. Major physiographic features of the Svalbard archipelago and sampling sites of seawater and pore fluids. Black closed circles: normal pore fluid sampling sites, green closed squared: freshening pore fluid sampling sites, purple closed triangle: brine pore fluid sampling site, red closed squares: seawater sampling sites.

deep (Hald et al., 2001). The mouth of the main fjord is almost entirely blocked from the open ocean by Akseløya Island. The bedrock is composed of Cretaceous and Tertiary shales, siltstones, and sandstones (Dallmann, 2015) and all glaciers in this fjord have experienced significant volume losses over the last century (Nuth et al., 2013).

Hornsund fjord is the southernmost fjord on western Spitsbergen with a length of 30 km and a maximum water depth of ~260 m (Frankowski and Ziola-Frankowska, 2014). The main bedrocks vary from Proterozoic metamorphic rocks at the fjord mouth in the west to Paleogene sedimentary rocks at the fjord head in the east (Dallmann, 2015).

The lithologies of the sediment cores from each Svalbard fjord have diverse characteristics. The sediment is mainly composed of gray to dark brown sandy mud, and ice-rafted debris (IRD) at Isfjorden (Yoon et al., 2006; Levitan et al., 2008); massive reddish brown mud or sandy mud with varying amounts of scattered clasts at Dicksonfjorden (Joo et al., 2019); reddish brown and dark to very dark grayish brown clayey silt with scattered clasts, as well as clayey silt with sandy mud at Tempelfjorden (Plassen et al., 2004); and homogeneous mud with scattered IRD, as well as reworked sediments with abundant shear structures and normal faults at Van Mijenfjorden (Hald et al., 2001). The bottom sediment of the Hornsund fjord area consists of sandy mud, laminated mud, homogeneous to bioturbated mud, and often sandy gravel (Gőrlich, 1986).

3. Materials and methods

3.1. Fluid sampling

Seven sediment cores were collected from five fjords in Spitsbergen by a gravity corer onboard the R/V Helmer Hanssen from the Arctic University of Norway in Tromsø (UiT) during the 2016 Expedition in July (Fig. 1; Table 1). Upon recovery, cores were immediately sectioned and capped with ca. one meter intervals on the core deck. We perforated holes in the core liner at 30–50 cm intervals to extract pore fluid using Rhizons attached to syringes on deck. To minimize contamination, all fluid sampling equipment (i.e., syringes, plastic vials, and rhizons) was stored in a 10% HCl bath for at least 4 h and then rinsed individually several times with ultrapure distilled water. Then, the sampling equipment was dried on a laminar flow clean bench. The extracted pore fluid was filtered through a 0.20 μm disposable polytetrafluoroethylene filter before collection for onboard and postcruise analyses. The pore fluid aliquots were transferred into

Table 1
Summaries of location, water depth, total core length, and maximum freshening ratio in each site.

Sample type	Site no.	Station	Fjord	Latitude (N)	Longitude (E)	Water depth (m)	Total core length (m)	Maximum freshening ratio (%)
Pore fluid	GC1	HH16-1178-GC-MF	Tempelfjorden	78° 24.8026′	17° 6.4911′	66.9	3.90	90.9
	GC2	HH16-1202-GC-MF	Dicksonfjorden	78° 43.6320′	15° 18.5839′	87.4	2.74	Brine
	GC3	HH16-1205-GC-MF	Isfjorden	78° 20.8134′	15° 17.1105′	259.5	4.66	0.0
	GC4	HH16-1209-GC-MF	Van Mijendjorden	77° 49.5664′	16° 21.216′	68.9	2.02	5.5
	GC5	HH16-1214-GC-MF	Van Mijendjorden	77° 47.7689′	15° 41.3312′	86.2	3.06	0.0
	GC6	HH16-1217-GC-MF	Hornsund	76° 58.9996′	16° 16.1584′	109.6	2.36	18.2
	GC7	HH16-1219-GC-MF	Hornsund	76° 58.6227′	15° 50.9790′	192.3	2.80	31.0
Seawater	S1	HH16-1181-CTD	Dicksonfjorden	78° 48.3129′	15° 21.7267′	38.8	36.1[a]	90.9
	S5	HH16-1191-CTD	Dicksonfjorden	78° 38.6120′	15° 16.9467′	101.0	98.7[a]	25.5
	S7	HH16-1211-CTD	Van Mijendjorden	77° 47.8121′	15° 41.0778′	86.5	85.7[a]	9.1
	S8	HH16-1221-CTD	Hornsund	76° 58.5246′	15° 50.9990′	192.5	191.3[a]	5.5

[a] Maximum CTD casting depth.

high density polyethylene vials for anion and cation analyses. The samples for cation analysis were acidified with ultrapure concentrated HNO_3 (~10 μl per 2 ml of sample). An additional subsample was collected in 2 ml septum screw-lid glass vials for water isotopes (δD and $\delta^{18}O$) analyses.

The seawater was also collected from Isfjorden, Van Mijenfjorden, and Hornsund fjord using a CTD/rosette system that holds twelve 5 L Niskin bottles (Seabird 911 Plus) (Fig. 1; Table 1). The seawater aliquots analyzing compositional and isotopic properties were preserved following the same protocols as described above for the pore fluid. All fluid samples were stored at 4 °C until analyses.

3.2. Chemical composition and isotope analyses

The chlorine (Cl^-) concentration and alkalinity of seawater and pore fluids were measured onboard during the 2016 Expedition. The Cl^- concentration and alkalinity were measured via titration with 0.1 M silver nitrate ($AgNO_3$) and 0.02 M HCl, respectively. The reproducibilities of Cl^- concentration and alkalinity were monitored by repeated analyses of the International Association of Physical Sciences of the Oceans (IAPSO) standard seawater and were < 2% and < 0.5%, respectively. Sulfate (SO_4^{2-}) was analyzed by ion chromatography (ICS-1500, Dionex) at the Korea Basic Science Institute (KBSI). Ammonium (NH_4^+) and phosphate (PO_4^{3-}) were measured spectrophotometrically (Shimazu UV-2450) at 640 nm and 885 nm at the Korea Institute of Geoscience and Mineral Resources, respectively.

Major and minor cations (Na^+, K^+, Mg^{2+}, Ca^{2+}, Ba^{2+}, Li^+, B, Sr^{2+}, Fe, Mn, and H_4SiO_4) were analyzed by inductively coupled plasma atomic emission spectrometry (Perkin Elmer Optima 8300) and inductively coupled plasma mass spectrometry (Thermo Fisher Scientific iCAP™) at the KBSI. The reproducibilities, estimated from repeated analyses of reference materials (SLRS-4 and NASS-5), were < 5%.

Water isotopes ($\delta^{18}O$ and δD) were determined with a VG prism stable isotope ratio mass spectrometer (IRMS) at the KBSI. The analytical reproducibilities were ± 0.1‰ for $\delta^{18}O$ and ± 1‰ for δD. All oxygen and hydrogen isotopic data are reported in the usual δ notation relative to Vienna Standard Mean Ocean Water (V-SMOW) (Eq. (1)).

$$\delta(‰) = \left(\frac{R_{Sample} - R_{Standard}}{R_{Standard}}\right) \times 1000 \quad (1)$$

where R represents the $^{18}O/^{16}O$ and D/H isotopic ratios of samples and standards.

Dissolved strontium and boron in seawater and pore fluids were separated for isotopic analyses using Sr-Spec columns (Eichrom-Sr resin) and B-specific exchange resin (Amberlite IRA 743), respectively. Strontium isotopic ratios ($^{87}Sr/^{86}Sr$) were measured using a Neptune multi-collector inductively coupled plasma mass spectrometer (MC-ICP-MS) (Thermo Finnigan, Bremen, Germany) at the KBSI. The measured $^{87}Sr/^{86}Sr$ ratios were normalized to $^{86}Sr/^{88}Sr = 0.1194$, and repeated measurements of NBS 987 yielded a value of 0.71025 ± 0.00002 ($2\sigma_{mean}$, $n = 24$). Boron isotopic ratios ($^{11}B/^{10}B$) were determined by a Neptune MC-ICP-MS (Thermo Finnigan, Bremen, Germany) on the PACITE platform at Institut Terre et Environnement de Strasbourg (ITES) (Université de Strasbourg) using a protocol adapted from Roux et al. (2015). The $^{11}B/^{10}B$ ratios are reported in the usual δ notation relative to NIST SRM 951 (Eq. (1)), and the repeated measurements of in-house reference material, which was seawater collected from Malibu Beach (California, USA), gave 39.43 ± 0.32‰ ($2\sigma_{mean}$, $n = 6$). The procedural reproducibility was 0.5‰ ($2\sigma_{mean}$).

3.3. Numerical modeling

We simulated a 4 m profile of dissolved Cl^- concentration using a customized MATLAB code similar to the one described in Sauer et al. (2021). We compared the modeling results with the observed concentration profiles from the three investigated sites (GC1, GC2, and GC7) to constrain the fluid advection rates and the time scales evolving from an assumed initial condition to a designated profile. The model was performed for 10,000 years. The following governing equation describes the conservation of bulk sediment volume:

$$\frac{\partial(M_x^t)}{\partial t} = \frac{\partial F_x^t}{\partial x} \quad (2)$$

M: mole/gram of material in bulk sediments as a function of depth and time.

F: volumetric flux of material (mole or gram/m^2 of bulk sediment/yr).

t and x: time (yr) and depth (m), respectively.

For dissolved Cl^-, the following equation was applied:

$$\frac{\partial(\phi_{f.x} S_x^t)}{\partial t} = \frac{\partial\left(D_x \frac{\partial(\phi_{f.x} S_x^t)}{\partial x} - (v_{f.x} + v_{ext.x})\phi_{f.x} S_x^t\right)}{\partial x} \quad (3)$$

$\phi_{f.x}$: pore fluid volume fraction as a function of depth (time invariance).

S_x^t: dissolved Cl^- concentrations as a function of depth and time.

$v_{f.x}$: pore fluid burial velocity as a function of depth (m bulk sediment/yr).

$v_{ext.x}$: external fluid velocity as a function of depth (m bulk sediment/yr).

D_x: diffusion coefficients as a function of depth (m^2 bulk sediment/yr).

The porosity, solute diffusion, advection of the sediment package, initial and boundary conditions used for modeling and results of sensitivity tests are detailed in the Supplementary Materials (e.g., Method, Fig. S1 and S2, Table S1).

Fig. 2. Profiles of Cl^-, SO_4^{2-} and alkalinity concentrations and molar ratios of NH_4^+/Cl^- ($x10^3$), Na^+/Cl^-, Mg^{2+}/Cl^-, K^+/Cl^-, Ca^{2+}/Cl^-, B/Cl^- ($x10^3$), Li^+/Cl^- ($x10^3$), Sr^{2+}/Cl^- ($x10^3$), and H_4SiO_4/Cl^- ($x10^3$) in seawater and pore fluids from the Svalbard fjords. The red dashed lines in the pore fluid profiles show bottom seawater value of Site S8 (water depth = 191.3 mbss).

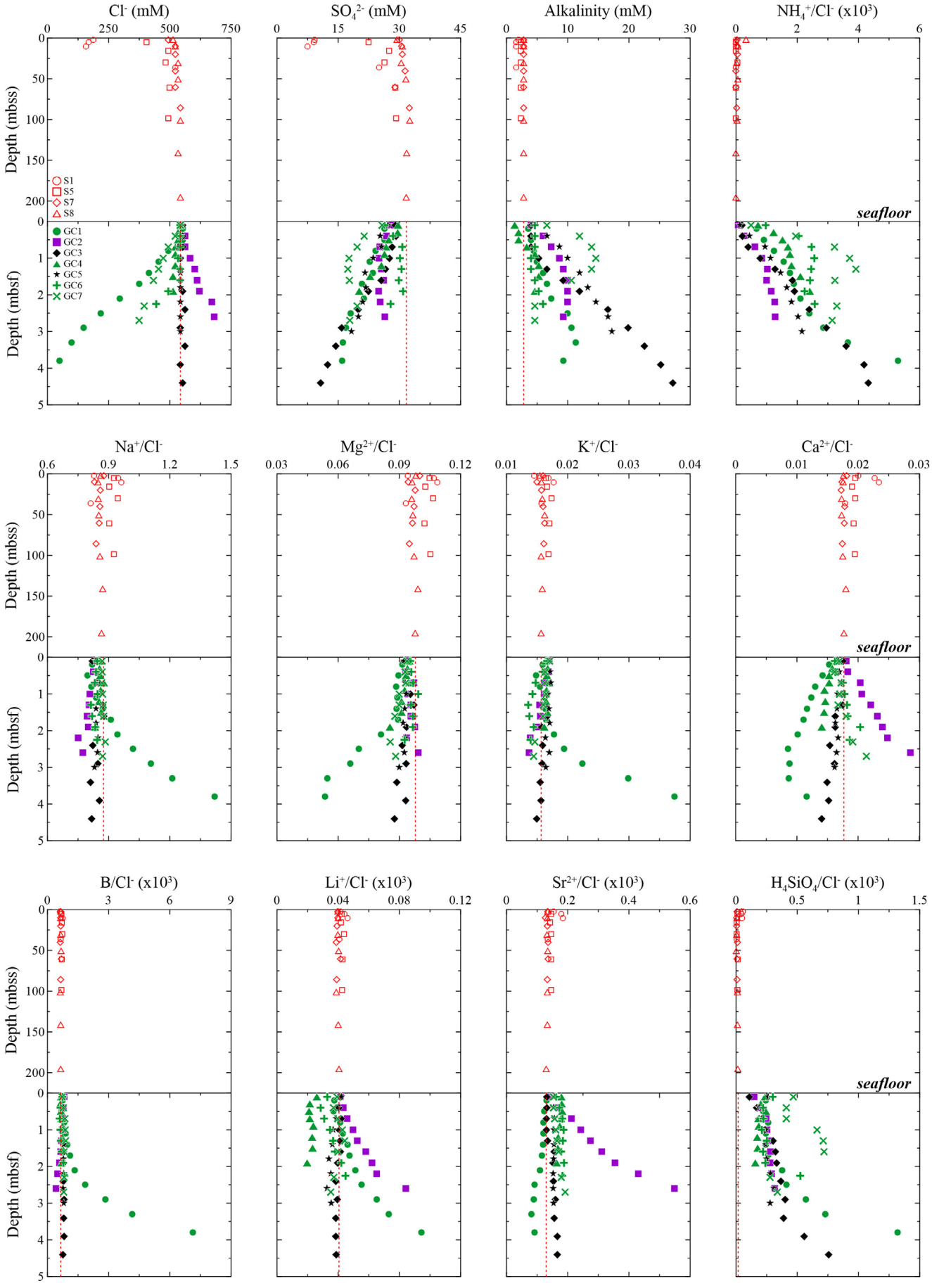
Cl- (mM)
SO4 2- (mM)
Alkalinity (mM)
NH4+/Cl- (x10³)
Na+/Cl-
Mg2+/Cl-
K+/Cl-
Ca2+/Cl-
B/Cl- (x10³)
Li+/Cl- (x10³)
Sr2+/Cl- (x10³)
H4SiO4/Cl- (x10³)
Depth (mbss)
Depth (mbsf)
seafloor
S1
S5
S7
S8
GC1
GC2
GC3
GC4
GC5
GC6
GC7

4. Results and discussion

The chemical and isotopic compositions of seawater and pore fluid samples are shown in Figs. 2 and 3 and Tables 2 and 3. In order to separate the effects of freshwater dilution and brine from the fluid data, we normalized the concentrations of most dissolved solutes (except for sulfate and alkalinity) to the Cl^- concentrations (Fig. 2). A conceptual model is presented in Fig. 4 to illustrate the hydrological process as well as the chemical reactions. This conceptual model is supported by our geochemical data and numerical modeling discussed in the following sections.

4.1. Causes of fluid freshening

4.1.1. Freshening of surface seawater due to runoff

The Cl^- concentrations and δD and $\delta^{18}O$ values of seawater samples generally increase as water depth increase at all four sampling sites (S1, S5, S7, and S8 from Figs. 2 and 3; Table 2). The most prominent increasing trend of Cl^- concentrations and isotopic signatures are observed in seawaters from Site S1 in Dicksonfjorden, characterized by the shallowest water depth of 38.8 m (Table 1; Fig. 1). The lowest values (Cl^- = 160 mM, δD = −68.1‰, and $\delta^{18}O$ = −9.7‰) are observed in the upper water column (<11 mbss, meters below sea surface). The shallowest samples collected at Sites S5, S7, and S8 also have distinctively lower Cl^- concentrations and isotopic signatures than those of the deepest samples. The differences in Cl^-, $\delta^{18}O$, and δD values between the surface and bottom seawater samples from Sites S1, S5, S7, and S8 decrease as the water depth at each site increases (Figs. 2 and 3; Table 2).

The different degrees of freshening from surface and shallow seawater reflect the contribution of freshwater to Svalbard fjords, which is greater at the sites closer to the heads of the fjords (i.e., sites with shallower water depths) (Fig. 2 and Table 1). In the Svalbard archipelago, the amount of freshwater discharged by runoff has been estimated to be at least 42% of the freshwater budget of surface seawater and the remaining freshwater was from the Barents Sea low-salinity Arctic Water in the 1990s (Beszczynska-Möller et al., 1997). Runoff mostly occurs during a few months from June to September as the rivers are mostly frozen for the rest of the year. Svalbard runoff mainly originates from snowmelt in June and July while the sources change to rainfall and glacier melt during August and September, respectively (Killingtveit et al., 2003). Our observations of the freshened surface seawater support that the runoff from precipitation, snow, and glaciers rapidly delivers freshwater to the coastal ocean from land.

4.1.2. Freshening of pore fluid due to the input of meteoric fluids

The Cl^- concentrations and $\delta^{18}O$ and δD values in pore fluids from Isfjorden, Tempelfjorden, Van Mijenfjorden, and Hornsund fjord show diverging downcore variations. The values in pore fluids from Sites GC3 (Isfjorden) and GC5 (Van Mijenfjorden) display a relatively constant downcore trend, ranging from 543 to 562 mM, −0.1‰ to 0.4‰, and −0.9‰ to 3.2‰ for Cl^- concentrations and $\delta^{18}O$ and δD values, respectively, which are close to the bottom seawater values at Site S8 (Cl^- = 543 mM, $\delta^{18}O$ = 0.4‰, and δD = 2.1‰) (Figs. 2 and 3; Tables 2 and 3). In contrast, Cl^- concentrations in pore fluids from Sites GC1 (Tempelfjorden), GC4 (Van Mijenfjorden), and GC7 (Hornsund fjord) steadily or rapidly decrease downcore with minimum values of 49 mM, 513 mM, and 375 mM at the bottom of the cores, respectively (Fig. 2; Table 3). At Site GC6 in Hornsund fjord, the Cl^- concentrations in the pore fluids remain almost constant down to 1.60 mbsf (meters below seafloor), from which it starts to decrease until it reaches 444 mM at 2.25 mbsf (Fig. 2; Table 3). Since the Cl^- concentration in the bottom seawater at Site S8 is ~543 mM (Fig. 2; Table 2), pore fluids from Sites GC1, GC4, GC6, and GC7 clearly illustrate fluid freshening. The maximum degrees of freshening at each site relative to the bottom seawater at Site S8 are estimated by the equation, $[Cl_{seawater} - Cl_{pore\ fluid}]/Cl_{seawater} \times 100]$, which yields 91%, 6%, 18%, 31% at Sites GC1, GC4, GC6, and GC7, respectively (Table 1).

The $\delta^{18}O$ and δD values in pore fluid from the top sediment at Sites GC1, GC4, GC6, and GC7 range from −0.1‰ to 0.3‰ and from −0.9‰ to 1.9‰, respectively, which are similar to the values from our representative bottom seawater sample (Tables 2 and 3). The downcore values of $\delta^{18}O$ and δD from these sites decrease with depth, similar to their respective Cl^- downcore trends. Different minimum values for $\delta^{18}O$ and δD at the bottom of the cores are observed: −13.2‰ and −92.3‰ at Site GC1, −0.5‰ and −3.4‰ at Site GC4, −2.2‰ and −14.5‰ at Site GC6, −3.6‰ and −24.3‰ at Site GC7, respectively (Figs. 2 and 3; Table 3).

In general, the freshening of pore fluid can be explained by meteoric water input, gas hydrate dissociation, and dehydration reactions, such as illitization and opal diagenesis (e.g., Kastner et al., 1991; Torres et al., 2004; Teichert et al., 2005; Kim et al., 2013, 2021). The freshening observed in the Svalbard fjords can be best explained by meteoric water input based on the positive correlation between water isotopes and Cl^-

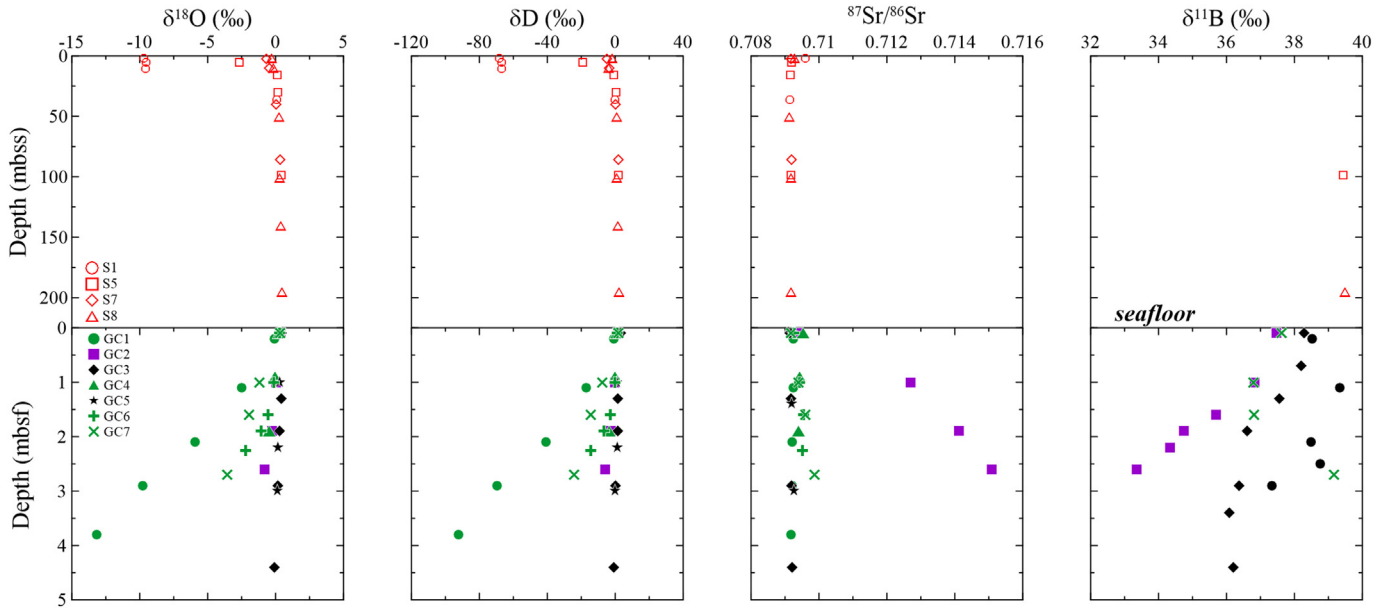

Fig. 3. Profiles of $\delta^{18}O$, δD, $^{87}Sr/^{86}Sr$, and $\delta^{11}B$ in seawater and pore fluids from the Svalbard fjords.

concentrations (Fig. 5). In addition, the measured $\delta^{18}O$ and δD values of pore fluids overlap with the local meteoric water line (LMWL) (http://www-naweb.iaea.org/napc/ih/HIS_resources_gnip.html) and their values at Site GC1 with the maximum freshening ratio are within the range of the present-day precipitation in the study area (Fig. 5). Other mechanisms, such as clay mineral dehydration and gas hydrate dynamics, cannot explain the observed data because clay mineral dehydration causes different fractionations of water isotopes, and gas hydrate dynamics have different correlations between Cl^- and δD values in our measured data (Fig. 5).

Considering the rapid decrease in the present cryosphere extent (Muckenhuber et al., 2016) and the large quantities of freshwater from both melting glaciers and snow to surface seawater (Beszczynska-Möller et al., 1997; Nuth et al., 2007, 2013; Fig. 2), the meteoric water signals in pore fluids can be mainly attributed to the freshwater from precipitation and the melting of glaciers, permafrost, and snow, which flows to the ocean through subsurface aquifers. Meteoric water sourced from melting glaciers, snow, and permafrost has been documented throughout the Arctic region (Hong et al., 2019 and see the references therein). Recently, Micallef et al. (2020) proposed that sub-glacial and pro-glacial injection is a primary mechanism causing the offshore freshened groundwater. Our observations from the Svalbard fjords can likely be explained by the same mechanism.

4.1.3. Heterogeneous subsurface freshening due to complicated hydrogeological conditions

Pore fluid freshening occurs in three of the fjords surveyed at the water depths of 66.9 m (Tempelfjorden; GC1), 68.9 m (Van Mijendjorden; GC4), and between 109.6 m and 192.3 m (Hornsund fjord; GC6 and GC7). Although Sites GC1 and GC4 have similar water depths, their maximum freshening degrees in pore fluid are contrastingly different (e.g., 91% versus 8% for the two sites). The drastically different pore fluid freshening can even be observed at the two adjacent sites in Hornsund fjord, Sites GC6 and GC7 (Fig. 2; Table 1). Unlike in the water column, where stronger freshening is observed at sites closer to land, the degree of pore fluid freshening cannot be correlated with water depth and distance from land. Rather, subsurface hydrogeology in each fjord, such as aquifer property and conduit connectivity, predominantly controls subseafloor freshening. Most Svalbard glaciers are polythermal, thus, they have a considerable meltwater retention capacity by refreezing in the porous snow and firn as the climate warms. Although the retention capacity is rapidly decreasing under recent and rapid climate warming, as well as a consequential reduction in cryosphere extent (Van Pelt et al., 2019), the amounts of meltwater discharge and its influence on the regional hydrology are still prominent and have high spatiotemporal variation in each Svalbard fjord (Christianson et al., 2015).

4.2. Subsurface brine as a result of submarine permafrost formation

Despite the low Cl^- concentrations in the pore fluids from several locations (Fig. 2; Tables 1 and 3), the core from Dicksonfjorden, Site GC2, has high Cl^- concentrations in the pore fluids, reaching a maximum Cl^- concentration of ~680 mM at the bottom of the core (Fig. 2; Table 3). Such a brine is characterized by light water isotopic signatures compared to the bottom seawater, which is negatively correlated with the Cl^- concentrations (Fig. 5). Recently, Charkin et al. (2017) described a mechanism, "cryogenic squeezing", to explain the observed brine bottom water on the Laptev Shelf. They proposed that the expulsion of dissolved solutes to the adjacent unfrozen water mass, as a result of rapid ice formation in the upper water column during the autumn-winter freezing season, could explain the observed brine. In terrestrial environments, brine water has also been reported in Siberia and Canada as a consequence of permafrost formation (Alexeev and Alexeeva, 2002, 2003; Shouakar-Stash et al., 2007; Stotler et al., 2009). We postulate a similar process in which the formation of submarine ice and/or permafrost in the sediment column in the geological past affects the pore fluid chemistry at Site GC2, even though the presence of submarine permafrost in the fjord has not been reported at present and thinning of permafrost toward the shore in the Svalbard region is expected in the warming ocean (Yoshikawa and Harada, 1995; Meier and Thannheiser, 2009). We speculate that submarine permafrost could have formed during a time when the maximum extent of the Barents Sea ice sheet covered the entire Svalbard archipelago, including the fjords (Ingólfsson and Landvik, 2013). As a result of submarine permafrost formation, enriched dissolved chemical species and light water isotopes (^1H and ^{16}O) were released from the freezing sediments into the unfrozen area, resulting in high concentrations of Cl^-, as well as other dissolved species, and depleted water isotopic signatures. Although the trends in water stable isotopes and Cl^- concentrations can also be explained by gas hydrate formation (Fig. 5B), this is rather unlikely because in situ gas hydrate was not found during the 2016 Expedition (KIGAM, 2016) and all sites did not penetrate the sulfate-methane transition zone to generate microbial methane, as is shown by the high SO_4^{2-} concentration in pore fluid (> 16 mM; Fig. 2 and Table 3) and the low methane concentrations

Table 2
Chemical and isotopic compositions of seawater from the Svalbard archipelago collected during the 2016 Expedition.

Site	Depth (mbss)	Cl^- (mM)	SO_4 (mM)	Alkalinity (mM)	NH_4^+ (μM)	PO_4^{3-} (μM)	Na^+ (mM)	K^+ (mM)	Mg^{2+} (mM)	Ca^{2+} (mM)	H_4SiO_4 (μM)	Ba^{2+} (μM)	B (μM)	Li^+ (μM)	Sr^{2+} (μM)	Mn (μM)	Fe (μM)	$\delta^{18}O$ (‰)	δD (‰)	$^{87}Sr/^{86}Sr$	$\delta^{11}B$ (‰)
S1	36.1	523	25.0	1.6	n.d.	0.0	450	8.2	48.7	9.3	n.d.	0.1	344.9	21.3	70.5	0.3	n.d.	0.1	−0.1	0.70914	38.5
	10.6	158	7.5	1.6	n.d.	0.9	130	2.8	17.1	3.7	n.d.	1.6	117.7	7.3	29.1	0.6	n.d.	−9.6	−67.0	–	–
	5.2	168	9.0	1.6	n.d.	n.d.	141	2.8	17.9	3.8	n.d.	1.5	115.2	7.4	30.0	0.6	n.d.	−9.5	−66.8	–	–
	2.3	187	9.2	2.0	n.d.	0.4	162	2.7	17.6	3.8	n.d.	1.6	116.2	7.8	29.0	0.6	n.d.	−9.7	−68.1	0.70959	39.3
S5	98.7	493	29.2	2.4	n.d.	0.4	423	9.2	51.9	9.6	3.1	0.5	341.3	21.0	71.7	0.2	n.d.	0.4	2.0	0.70917	39.4
	61.2	498	29.1	2.4	n.d.	0.7	429	9.5	51.0	9.6	3.8	0.3	351.9	21.3	72.5	0.4	n.d.	–	–	–	–
	30.2	483	26.4	2.4	22.3	n.d.	408	9.1	51.5	9.4	n.d.	0.3	354.7	21.2	70.8	0.2	n.d.	0.2	0.5	–	–
	15.7	493	27.5	2.4	0.0	0.2	422	9.4	50.6	9.4	n.d.	0.3	345.0	20.6	70.1	0.3	n.d.	0.1	−0.8	0.70915	–
	5.2	405	22.5	2.4	0.0	n.d.	345	9.3	42.4	7.9	0.0	0.3	279.7	17.1	58.9	0.3	n.d.	−2.7	−19.2	0.70920	–
S7	85.7	543	32.4	2.8	14.4	0.4	480	8.7	51.5	9.4	0.0	0.1	347.3	21.2	72.2	0.5	n.d.	0.3	2.0	0.70920	38.3
	60.6	523	28.9	2.8	n.d.	1.1	456	8.5	50.4	9.3	5.0	0.1	355.0	21.7	71.0	0.3	n.d.	–	–	–	–
	40.3	523	31.4	2.8	n.d.	0.4	460	8.3	50.8	9.3	n.d.	0.1	332.8	20.3	70.9	0.2	n.d.	0.0	0.1	–	38.2
	20.1	523	30.7	2.8	26.2	0.4	459	8.2	51.1	9.0	n.d.	0.1	336.4	20.5	69.5	0.4	n.d.	–	–	–	–
	10.2	523	30.5	2.8	22.3	0.5	462	7.8	49.4	9.1	14.7	0.1	339.5	20.7	66.8	0.5	n.d.	−0.5	−3.5	–	37.6
	2.4	493	30.0	2.8	18.3	0.4	432	7.9	49.3	9.0	n.d.	0.1	323.7	19.6	66.8	0.4	n.d.	−0.7	−4.9	0.70918	–
S8	191.3	543	31.7	2.8	n.d.	n.d.	475	8.5	53.1	9.6	n.d.	0.1	353.9	22.0	70.3	0.2	n.d.	0.4	2.1	0.70918	39.5
	140.9	533	31.8	2.8	n.d.	0.7	466	8.4	52.8	9.6	n.d.	0.1	349.1	21.3	71.4	0.2	n.d.	0.4	1.4	–	–
	101.2	543	32.6	2.8	18.3	0.2	478	8.5	52.7	9.5	n.d.	0.0	345.1	21.1	72.5	0.2	n.d.	0.3	1.0	0.70917	–
	50.5	533	31.5	2.8	30.1	0.2	469	8.6	51.5	9.2	n.d.	0.1	354.1	21.5	71.8	0.2	n.d.	0.3	0.7	0.70913	–
	30.4	533	30.4	2.8	14.4	n.d.	467	8.4	51.2	9.2	n.d.	0.1	345.5	21.1	70.3	0.2	n.d.	–	–	–	–
	10.1	523	30.8	2.8	30.1	n.d.	460	8.2	50.3	9.2	7.7	0.1	338.8	21.0	69.7	0.2	n.d.	−0.2	−3.7	–	–
	2.0	513	29.4	2.8	166.7	0.4	448	7.9	50.4	9.0	2.3	0.1	330.2	20.4	68.8	0.3	n.d.	−0.3	−2.0	0.70927	–

–: No measurement.
n.d.: Below detection limit.

Table 3
Chemical and isotopic compositions of pore fluids from the Svalbard archipelago collected during the 2016 Expedition.

Site	Depth (mbsf)	Cl^- (mM)	SO_4 (mM)	Alkalinity (mM)	NH_4^+ (mM)	PO_4^{3-} (μM)	Na^+ (mM)	K^+ (mM)	Mg^{2+} (mM)	Ca^{2+} (mM)	H_4SiO_4 (μM)	Ba^{2+} (μM)	B (μM)	Li^+ (μM)	Sr^{2+} (μM)	Mn (μM)	Fe (μM)	$\delta^{18}O$ (‰)	δD (‰)	$^{87}Sr/^{86}Sr$	$\delta^{11}B$ (‰)
GC1	0.20	553	26.4	3.6	0.4	0.0	482	8.8	50.5	8.4	135.3	0.3	407.6	20.7	83.0	10.1	321.0	−0.1	−0.9	0.70923	38.5
	0.50	553	26.3	4.0	0.5	1.6	486	8.2	49.5	7.9	121.9	0.2	383.8	20.4	82.3	8.5	280.4	–	–	–	–
	0.80	493	24.2	4.5	0.6	0.0	438	7.6	43.6	6.4	129.9	0.2	400.1	20.4	83.9	4.2	170.5	–	–	–	–
	1.10	454	22.7	5.0	0.7	0.0	404	7.4	40.3	5.6	110.4	0.2	408.6	19.5	82.0	4.7	133.8	−2.5	−17.1	0.70923	39.3
	1.40	414	23.5	6.0	0.7	0.0	377	6.8	36.7	4.8	101.4	0.2	403.6	19.1	84.4	3.6	57.7	–	–	–	–
	1.70	375	20.8	6.6	0.7	0.0	341	6.2	33.5	4.2	98.1	0.1	410.9	17.8	81.6	3.5	73.1	–	–	–	–
	2.10	296	21.3	7.3	0.6	0.0	286	5.3	23.9	3.0	111.3	0.2	394.0	15.1	81.8	2.4	50.9	−5.9	−40.8	0.70921	38.5
	2.50	217	18.0	10.0	0.5	3.7	224	4.2	15.2	1.9	89.2	0.1	403.0	12.0	80.7	1.4	12.2	–	–	–	38.8
	2.90	148	16.9	10.6	0.4	20.5	167	3.3	9.7	1.3	84.4	0.1	419.9	9.6	81.8	1.4	0.2	−9.8	−69.5	0.70921	37.3
	3.30	99	16.1	11.3	0.4	46.1	126	3.0	5.4	0.9	71.8	0.1	410.4	7.2	80.5	1.2	2.3	–	–	–	–
	3.80	49	16.0	9.3	0.3	95.1	82	1.8	2.6	0.6	65.1	0.1	351.7	4.7	81.4	0.6	4.5	−13.2	−92.3	0.70918	–
GC2	0.10	543	27.9	4.0	0.0	11.4	472	9.2	50.8	9.8	79.6	0.5	444.3	22.6	75.5	189.8	19.2	0.4	1.7	0.70936	37.5
	0.40	562	26.8	6.0	0.1	25.1	487	9.5	52.3	10.3	116.0	0.3	436.9	24.3	94.3	158.2	30.4	–	–	–	–
	0.70	562	25.2	7.3	0.3	52.5	478	9.1	54.7	11.5	138.7	0.3	415.3	25.8	119.4	118.9	40.1	–	–	–	–
	1.00	582	25.0	8.6	0.5	62.4	497	9.4	55.0	12.0	146.7	0.3	423.0	28.8	141.5	102.7	41.6	0.1	0.0	0.71269	36.8
	1.30	602	25.6	9.3	0.6	61.9	511	9.3	57.6	13.3	167.1	0.3	411.4	31.5	165.3	92.7	44.7	–	–	–	–
	1.60	612	26.1	10.0	0.6	53.8	518	9.5	58.6	14.2	172.1	0.3	400.6	35.6	190.1	84.3	47.5	–	–	–	35.7
	1.90	622	24.9	10.0	0.7	40.1	520	9.3	60.6	14.9	172.7	0.3	372.2	38.7	219.9	69.8	30.9	−0.3	−2.5	0.71413	34.7
	2.20	671	25.3	10.0	0.8	34.5	562	9.3	62.8	16.6	195.4	0.3	338.8	43.7	289.0	56.4	46.1	–	–	–	34.3
	2.60	681	26.5	9.3	0.9	21.3	559	9.3	67.6	19.4	215.8	0.2	286.3	57.4	373.2	41.3	83.2	−0.8	−5.8	0.71509	33.4
GC3	0.10	553	29.0	4.0	0.1	0.0	483	9.4	51.2	9.7	60.4	0.3	414.7	22.9	73.0	10.6	22.4	0.4	3.2	0.70915	38.3
	0.40	553	29.2	4.0	0.1	2.0	483	9.0	52.3	9.2	93.6	0.2	406.4	22.4	72.8	4.1	28.4	–	–	–	–
	0.70	553	28.2	4.0	0.2	5.9	480	9.2	52.2	9.6	105.2	0.2	412.6	23.2	72.2	5.6	26.8	–	–	–	38.2
	1.00	543	27.5	5.3	0.4	29.8	471	9.0	51.8	9.4	126.4	0.2	411.9	22.2	71.3	6.9	28.0	–	–	–	–
	1.30	543	26.7	6.6	0.7	43.1	469	9.0	52.7	9.5	164.7	0.2	405.5	22.4	73.3	8.4	28.0	0.4	1.6	0.70918	37.6
	1.60	543	25.6	9.3	1.0	58.1	470	9.0	52.7	8.8	175.4	0.2	430.0	22.5	84.8	10.5	30.3	–	–	–	–
	1.90	553	22.5	11.9	1.1	92.8	478	8.7	51.6	9.0	183.5	0.2	438.6	21.9	84.5	11.2	19.2	0.3	1.6	–	36.6
	2.40	563	25.5	16.6	1.3	139.8	509	9.0	51.4	8.6	205.2	0.2	445.1	21.7	86.8	11.2	19.7	–	–	–	–
	2.90	543	28.5	19.9	1.6	168.1	491	8.6	50.7	8.8	217.9	0.2	450.7	21.5	87.2	10.4	15.6	0.2	0.1	0.70920	36.4
	3.40	562	14.4	22.6	2.0	172.4	487	8.7	49.9	8.4	219.3	0.2	449.8	21.6	87.9	9.2	5.2	–	–	–	36.1
	3.90	543	12.5	25.2	2.3	204.5	465	8.5	50.5	8.3	303.4	0.3	446.3	20.8	90.5	9.5	10.9	–	–	–	–
	4.40	553	10.7	27.2	2.4	210.9	478	8.3	48.4	7.8	418.4	0.3	427.5	21.4	91.8	9.3	2.5	−0.1	−0.9	0.70921	36.2
GC4	0.10	543	29.7	1.3	0.4	12.7	473	8.9	51.5	8.9	128.6	0.4	365.5	14.1	97.0	167.2	896.0	0.2	0.8	0.70952	–
	0.30	533	29.5	2.0	0.6	13.1	467	8.9	50.0	8.4	107.2	0.3	337.1	11.4	96.4	60.6	872.5	–	–	–	–
	0.50	533	27.4	2.0	0.8	6.7	464	8.9	49.8	8.2	130.3	0.3	352.6	11.1	97.1	36.5	724.3	–	–	–	–
	0.70	523	26.7	3.3	0.9	3.7	455	8.9	49.7	8.0	95.3	0.3	354.7	11.3	93.2	33.3	580.1	–	–	–	–
	0.90	523	26.3	4.6	0.9	0.0	459	8.7	48.4	7.6	97.3	0.3	384.8	12.4	91.0	43.4	496.3	0.0	−0.1	0.70942	–
	1.20	523	25.6	5.3	0.9	0.0	459	8.6	47.6	7.7	89.8	0.2	377.0	12.0	88.2	27.6	394.3	–	–	–	–
	1.50	513	22.9	5.3	1.1	0.0	446	8.6	46.7	7.4	90.1	0.2	374.7	11.9	86.1	18.9	317.7	–	–	–	–
	1.90	513	20.2	4.6	1.2	0.0	446	8.3	43.8	7.2	81.1	0.2	348.3	10.1	84.2	9.7	305.2	−0.5	−3.4	0.70941	–
GC5	0.10	543	27.2	4.0	0.1	8.0	473	9.2	50.1	9.1	142.7	0.4	436.0	22.8	84.6	66.8	159.5	0.3	1.7	0.70917	–
	0.40	543	25.3	6.6	0.2	8.4	471	9.3	50.6	9.2	103.3	0.3	425.5	21.5	83.1	64.3	152.4	–	–	–	–
	0.70	533	25.6	8.6	0.5	9.7	466	9.2	49.4	9.2	111.8	0.2	424.3	20.7	83.3	58.3	150.2	–	–	–	–
	1.00	543	23.6	10.0	0.6	8.4	471	9.1	50.7	9.0	131.4	0.2	435.3	19.9	84.0	64.6	145.6	0.3	0.9	–	–
	1.40	543	21.6	11.9	0.8	15.3	469	9.2	50.2	9.0	131.4	0.2	438.2	19.7	83.9	67.6	143.9	–	–	0.70919	–
	1.80	543	21.7	13.3	0.9	11.9	472	9.3	49.8	8.8	134.9	0.2	423.1	18.4	83.4	58.8	135.6	–	–	–	–
	2.20	543	21.0	14.6	1.0	26.4	470	8.9	50.4	9.1	152.0	0.2	437.5	19.0	83.0	58.9	145.4	0.2	1.1	–	–
	2.60	543	19.9	16.6	1.1	5.0	471	9.2	50.1	8.9	168.1	0.2	409.3	17.8	82.5	66.4	88.3	–	–	–	–
	3.00	543	18.2	17.2	1.2	5.9	471	8.9	48.8	8.8	151.5	0.2	435.9	19.3	83.1	93.6	50.9	0.1	0.0	0.70926	–
GC6	0.10	543	26.4	4.6	0.5	0.0	469	9.1	51.8	8.8	162.2	0.4	401.3	17.9	88.4	68.8	432.9	0.3	1.3	0.70926	–
	0.40	543	28.4	4.6	1.1	0.0	473	8.6	52.0	8.8	119.8	0.2	355.3	15.5	93.7	19.0	527.0	–	–	–	–
	0.70	543	30.7	4.6	1.3	0.0	475	8.0	52.5	9.5	122.5	0.2	331.5	16.8	99.2	13.0	587.8	–	–	–	–
	1.00	533	30.2	4.0	1.4	2.0	463	7.6	52.9	9.5	111.7	0.2	344.4	18.5	99.8	11.3	560.8	−0.2	−0.2	0.70943	–
	1.30	543	30.5	4.0	1.3	2.4	475	7.4	51.9	9.9	136.9	0.2	366.3	20.0	100.1	12.0	566.6	–	–	–	–
	1.60	543	29.8	4.6	1.3	0.0	474	7.5	52.4	9.9	119.6	0.2	378.4	20.6	97.3	11.5	538.5	−0.5	−2.8	0.70955	–
	1.90	493	30.9	5.3	1.1	0.0	437	7.1	47.7	10.1	118.5	0.2	385.8	20.8	93.1	16.0	406.7	−1.1	−6.5	–	–
	2.25	444	27.9	6.0	1.1	0.0	400	6.2	41.1	8.3	233.0	0.2	376.0	19.9	81.4	15.2	279.0	−2.2	−14.5	0.70952	–
GC7	0.10	543	25.7	6.6	0.3	69.2	471	9.3	50.8	9.2	253.5	0.2	396.2	21.4	83.7	16.5	93.1	0.3	1.9	0.70917	37.6
	0.40	523	21.4	11.9	1.0	32.0	454	8.6	48.5	8.4	214.5	0.2	405.3	19.3	80.7	17.5	179.3	–	–	–	–
	0.70	493	19.7	13.9	1.6	0.7	428	8.0	46.0	8.5	202.7	0.2	421.5	19.6	77.6	17.2	97.8	–	–	–	–
	1.00	474	17.7	14.6	1.8	44.0	413	7.8	42.6	8.0	313.5	0.2	413.8	20.2	76.3	16.0	121.5	−1.2	−7.6	0.70940	36.8
	1.30	454	17.4	13.9	1.8	51.2	397	7.3	40.8	7.6	323.4	0.2	404.0	20.1	74.9	16.0	121.7	–	–	–	–
	1.60	434	17.8	10.6	1.4	20.0	380	6.9	38.1	7.9	311.7	0.2	354.6	17.4	74.1	15.2	187.5	−2.0	−14.3	0.70961	36.8
	2.30	395	19.7	4.6	1.3	0.0	349	5.8	33.7	7.6	109.1	0.3	323.5	14.7	70.7	8.7	250.3	–	–	–	–
	2.70	375	17.9	4.6	1.2	2.0	327	5.4	33.1	8.0	126.4	0.2	300.5	13.2	72.1	10.2	257.8	−3.6	−24.3	0.70987	39.2

–: No measurement.

(KIGAM, 2016). The observed pore fluid profiles at Site GC2 thus most likely reflect mixing between local seawater and brine resulting from submarine permafrost formation.

Seawater intrusion can alter the pore fluid composition in shallow sediments of the fjords. If the supply of either terrestrial freshwater or marine brine has been terminated for sufficient time (a few hundred years based on the modeling results; Fig. 6), the diffusion of seawater from the seafloor slowly erases all anomalous geochemical signals and results in identical downcore chemical and isotopic values of the pore fluids at Sites GC3 and GC5. The pore fluid chemistry at Site GC2 did

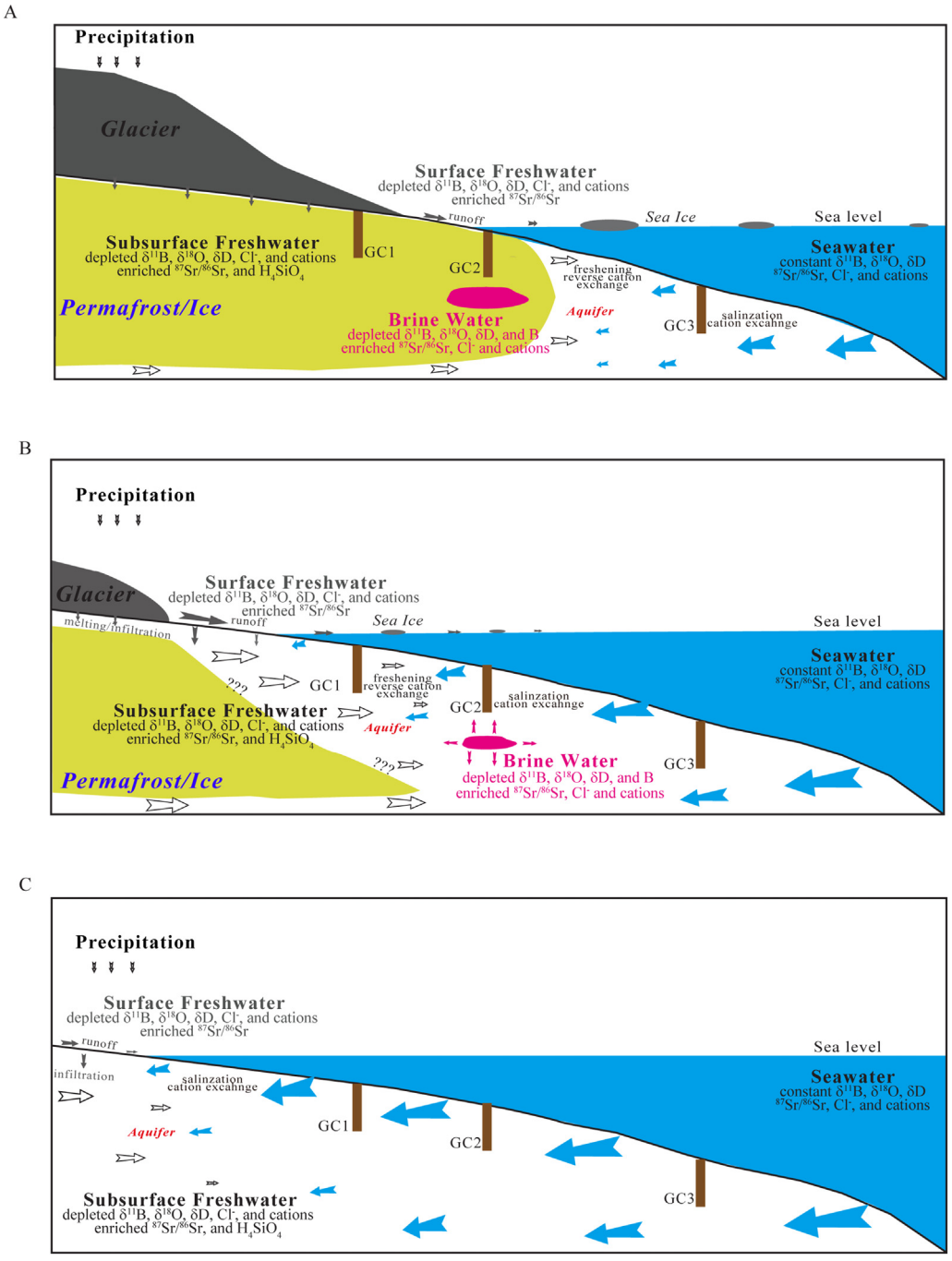

Fig. 4. Conceptual model illustrating the hydrological processes, chemical reactions, and characteristics of each fluid source at Isfjord interacting with the hydrosphere-cryosphere-lithosphere during the cooling period of the late Holocene (A), at present (B), and in the future (C). Subsurface freshwater is the sum of the groundwater and meltwater of the cryosphere (i.e., glacier, permafrost, ice). The arrow size shows the relative fluid flux.

not corroborate any evidence for freshening by terrestrial freshwater discharge and/or by the degradation of permafrost or ice. Instead, it indicates the predominant mixing of present-day seawater and residual brine fluid in the deep sediment column without (or with slight) terrestrial freshwater discharge. Hence, the brine signals at Site GC2 are indirect evidence for the influence of submarine cryosphere formation in the deeper parts of Dicksonfjorden, likely during the cooling period of the late Holocene (see Section 4.3 for further discussion on timing). This finding may also strengthen our interpretation that the interaction between the hydrosphere and cryosphere in each Svalbard fjord impacts the seawater and pore fluid chemistry.

4.3. Time scales of fluid freshening and brine formation

The early Holocene was a relatively warm period with a strong inflow of warm Atlantic Water leading to reduced sea ice formation and glacier extent in Isfjord and its branches (Peral et al., 2022). Counterintuitively, the regional sea level during this warm period was lower than that during the glacial period due to postglacial crustal rebound (Svendsen and Mangerud, 1997; Forwick and Vorren, 2009; Mangerud and Svendsen, 2018; van der Bilt et al., 2018; Joo et al., 2019; Farnsworth et al., 2020), which could have led to the production of brine pore fluid as the shallow water depth could have enhanced the formation of (submarine) permafrost

in this area. This phenomenon, however, does not explain the brine observed at Site GC2, as sea level in Dicksonfjorden was higher during the early Holocene than at the present level by at least ~90 m (Forman et al., 2004). Rather, we postulate that the brine fluid was produced in the sediment column through submarine permafrost formation during the cooling periods of the late Holocene.

As the insolation and the inflow of Atlantic Water decreased from ca. 9 ka BP, cooler conditions occurred during the late Holocene with glacier readvances at different times (Mangerud and Svendsen, 2018; van der Bilt et al., 2018; Joo et al., 2019). This occurrence is also expected to have enhanced shorefast sea ice formation and/or more permanent sea ice cover in central Isfjorden and its branches during the late Holocene (e.g., Forwick and Vorren, 2009; Baeten et al., 2010). Indeed, Site GC2 records a period with intensive sea ice formation from 1.53 mbsf (~3 ka BP) based on the abundance of ice-rafted debris (Joo et al., 2019). Moreover, the glaciers on Svalbard reached their maximum Holocene extent by the termination of the LIA in the beginning of the 1920s (Hagen et al., 2003) and the maximum brine production in the water column also correlated with the Dark Ages Cold Period (1500–1100 yr BP) and the LIA (600–100 yr BP) (Rasmussen and Thomsen, 2014). Therefore, we suggest that these cooling conditions in the late Holocene might have led to the development of submarine permafrost at Site GC2. Such a time scale is consistent with the numerical modeling result showing that at least ca. 400 years are needed for the downcore dissolved Cl^- profile at Site GC2 to evolve from an initial seawater composition to a profile that is extensively influenced by brine (Fig. 6). In contrast, the freshwater signatures observed at Sites GC1, GC4, GC6, and GC7 can be mainly explained by the discharge of terrestrial freshwater into the ocean through subsurface conduits associated with the melting of glaciers and permafrost on land that has been occurring for a few centuries. Possible conduits include porous media, fractures (e.g., the Hornsund fracture zone adjacent to GC6 and GC7), and widely distributed karst formation (Dallmann, 2015). Although we are not able to know the exact subsurface flow conduits, the presence of geological features supports our inference. According to the simulation results of the downcore Cl^- profiles at Sites GC1 and GC7, it takes at least ca. 500 years for the profiles to evolve from an initial seawater condition, although the Cl^- profiles slightly adjust again during the last century due to the high sedimentation rate assigned in the model, which results in faster burial of the pore fluids (Figs. 6 and S2). During the same period, the upward fluid advection (due to processes such as overpressure) is slower than sedimentation, and the downcore Cl^- profiles are thus slightly concave-upward (Fig. 6B). We also estimate slightly higher upward fluid advection rates, specifically <0.2 cm/yr at Site GC1 and ~ 0.5 cm/yr at Site GC7, compared to that at Site GC2 (Fig. S2). Without other age

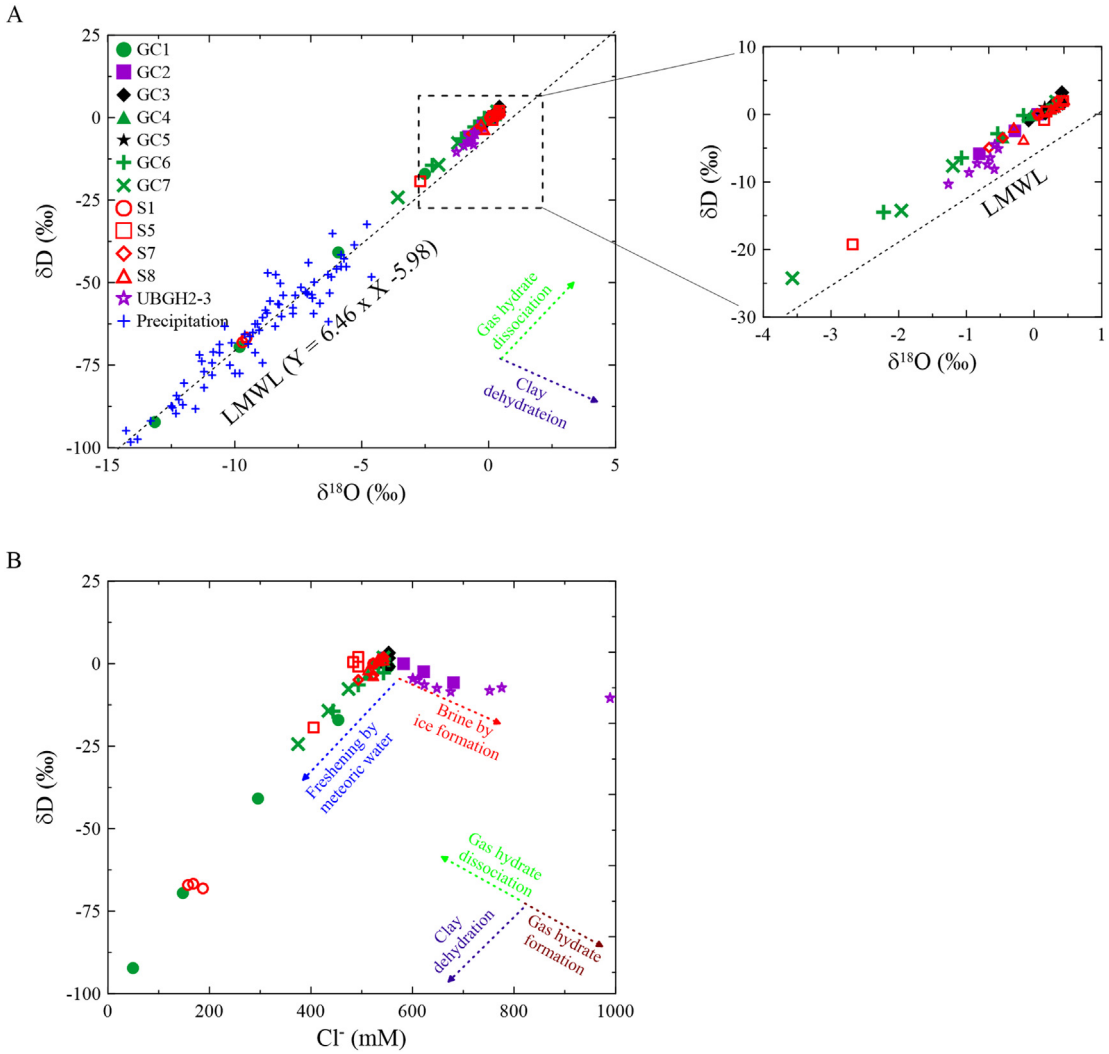

Fig. 5. Scatter plots of A) δD versus $\delta^{18}O$ and B) δD versus Cl^- in seawaters, pore fluids, and precipitation from the Svalbard fjords, in comparison with pore fluids from Site UBGH2–3 in the Ulleung Basin, showing enrichment of Cl^- with depleted δD and $\delta^{18}O$ values by rapid hydrate formation. LMWL is a local meteoric water line at Isfjord, Norway, from the Global Network of Isotopes in precipitation (http://www-naweb.iaea.org/napc/ih/IHS_resources _gnip.html). UBGH2–3 data came from Kim et al. (2013).

constraints, it is difficult to precisely determine the exact timing of freshwater arrival. Nonetheless, our modeling results suggest that such a freshened groundwater circulation has continued for a few centuries.

4.4. Ion exchange reaction and seawater intrusion

After normalization to the Cl^- concentration, each dissolved cation profile shows site-distinctive variation, which can be largely divided into three groups. The first group, which includes Site GC1 with a maximum freshening ratio, has distinctly higher $(Na^+ + K^+)/Cl^-$ and lower $(Ca^{2+} + Mg^{2+})/Cl^-$ ratios than the ratios from the representative bottom seawater at Site S8 (Fig. 7). Although the bedrock of Tempelfjorden is partly composed of carbonate-rich rock (Dallmann, 2015), the observed decreasing downcore trend of $(Ca^{2+} + Mg^{2+})/Cl^-$ in pore fluids at Site GC1 (Fig. 7) suggests that the pore fluid chemistry is not controlled by the carbonate dissolution. We propose that salinity-dependent reverse cation exchange is the most plausible mechanism to explain the trends observed in these elemental ratios because the shallow sediment of Tempelfjorden is mainly composed of clayey silt (Plassen et al., 2004). The freshening of pore fluids at Site GC1 leads to the exchange that Na^+ and K^+ on the exchanger complex are replaced by Ca^{2+} and Mg^{2+}, as expressed by the following equation (Appelo and Postma, 2005):

$$\left(Ca^{2+}, Mg^{2+}\right) + (Na^+, K^+) - X \leftrightarrow 2\,(Na^+, K^+) + \left(Ca^{2+}, Mg^{2+}\right) - X \qquad (4)$$

where *X* represents the complex exchanger (sediment and/or aquifer).

Consequently, $(Na^+ + K^+)/Cl^-$ and $(Ca^{2+} + Mg^{2+})/Cl^-$ ratios in pore fluids become higher and lower, respectively, than the seawater ratios (Fig. 7). Intruded seawater as the result of the loss in cryosphere extent can influence the properties of shallower pore fluid. However, among the study sites, Site GC1 is located at the most landward part of the fjord, which is supposed to be the least influenced by seawater intrusion. The Sr^{2+}/Cl^- ratios in pore fluids are also lower than the seawater ratio, which can be similarly explained by reverse cation exchange due to the similar chemical properties between Sr^{2+} and Ca^{2+} (Figs. 2 and 7). Interestingly, B/Cl^- and Li^+/Cl^- in pore fluids increase as the sediment depth increases at Site GC1 and show higher values than those of seawater. B/Cl^- and Li^+/Cl^- also correlate well with $(Na^+ + K^+)/Cl^-$, NH_4^+/Cl^- and H_4SiO_4/Cl^- (Figs. 2, 7, and S3). As opposed to the increasing downcore trends in the elemental ratios, the $\delta^{11}B$ values in the pore fluids decrease downcore (Fig. 3; Table 3). This indicates that the degradation of organic matter releases dissolved boron that is enriched with light boron isotope (^{10}B) through B-NH_4^+ exchange in clay during early diagenesis in marine sediment (Teichert et al., 2005), which also supports the occurrence of reverse ion exchange reactions involving NH_4^+.

For Site GC2, where brine is present and the clay content is >20% (Joo et al., 2019), we propose that cation exchange (the opposite of reverse cation exchange in Eq. (4) from right to left) could explain the higher $(Ca^{2+} + Mg^{2+})/Cl^-$ and lower $(Na^+ + K^+)/Cl^-$ ratios observed in the pore fluids at Site GC2. In this case, Ca^{2+} and Mg^{2+} on the exchanger complex are replaced by Na^+ and K^+ as the brine fluid appears in the sediment. The values of Sr^{2+}/Cl^- and Li^+/Cl are also higher than those of the bottom seawater at Site S8, which means that Sr^{2+} and Li^+ are released into the pore fluid by water-rock interactions, including ion exchange reactions (Figs. 2 and 7). These water-rock interactions or carbonate precipitation can influence boron chemistry because boron can be either adsorbed or desorbed, respectively, during these reactions (Kowalski and Wunder, 2018; Hong et al., 2022). However, little variation in alkalinity below 1.30 mbsf at Site GC2 is observed and points to no carbonate precipitation. Besides, B/Cl^- exhibits negative correlations with NH_4^+/Cl^- and H_4SiO_4/Cl^- ratios and suggests that B is not affected by water-rock interactions. In addition, the $\delta^{11}B$ value decreases with increasing depth and has the lightest at the bottom of Site GC2 among the analyzed pore fluid samples (Figs. 2, 3, and S3; Table 3). These results suggest that the two reactions can be excluded as the major factors controlling fluid B chemistry at Site GC2. Rather, the source of the brine fluid is likely to have a very low B concentration with depleted $\delta^{11}B$ signatures from the deep-seated sediment at Site GC2. Both the B concentration and B/Cl^- ratio in pore fluids from Site GC2 negatively correlate with $\delta^{11}B$ (R^2 = 0.90 and 0.97 for B and B/Cl^-, respectively) (Fig. 8; Table 3), which is consistent with our interpretation for the boron source. Assuming that the pore fluid from Site GC2 is a result of binary mixing between a brine fluid with a low boron concentration and seawater with B/Cl^- and $\delta^{11}B$ values from the sample at 0.10 mbsf of this site, the Cl^- concentration and $\delta^{11}B$ in the brine fluid are estimated to be 844 mM and 28.9‰, respectively. Similarly, the estimated $\delta^{18}O$ and δD values for the same brine are −2.0‰ and − 13.7‰, respectively (Fig. 8).

The third group has an invariable downcore trend of cations/Cl^- (Figs. 2 and 7). However, $(Na^+ + K^+)/Cl^-$ is similar to/or slightly higher than that of the bottom seawater from Site S8, whereas $(Ca^{2+} + Mg^{2+})/Cl^-$ and Li^+/Cl display slightly lower values compared to the bottom seawater (Fig. 7). These results imply that the pore fluid from this group is slightly altered by the processes that are responsible for the trends in Group 1.

4.5. Lithosphere influence on the fluid $^{87}Sr/^{86}Sr$ value

The $^{87}Sr/^{86}Sr$ values in pore fluids from Sites GC3 and GC5 range from 0.70914 to 0.70926 (Figs. 3 and 8; Table 3), which are similar to the bottom seawater value from Site S8 (~0.70918; Table 2) indicating that the pore fluid is mostly from the ambient bottom seawater. This interpretation is consistent with the fluid source inferred from the Cl^- and water isotope data (see Section 4.1). In contrast, these $^{87}Sr/^{86}Sr$ values in pore fluids from Sites GC2, GC4, GC6, and GC7 are higher than that of the bottom seawater from Site S8 (Figs. 3 and 8; Tables 2 and 3). In particular, a maximum $^{87}Sr/^{86}Sr$ value of 0.71504 is observed in pore fluids from Site GC2, which is abnormally higher than that of bottom seawater from Site S8 and pore fluids from Sites GC3 and GC5 (Figs. 3 and 8; Tables 2 and 3). Interestingly, while pore fluids from Sites GC2, GC4, GC6, and GC7 have higher Sr^{2+}/Cl ratios than the bottom seawater from Site S8 (0.00013) (Figs. 2 and 7), the correlation between $^{87}Sr/^{86}Sr$ and Sr^{2+}/Cl^- ratios at these sites shows three different trends: a positive correlation at Sites GC2 and GC7 (R^2 > 0.82), a negative correlation (R^2 = 0.69) at Site GC4, and little correlation at Site GC6 (Fig. 8). These different correlations do not correspond to the changes in dissolved Cl^- concentrations at these sites, and thus they indicate that $^{87}Sr/^{86}Sr$ values in pore fluids from the Svalbard fjords are influenced by sources enriched in radiogenic ^{87}Sr. We propose that the high $^{87}Sr/^{86}Sr$ values in the pore fluids reflect the leaching of bedrocks during fluid migration. The bedrock of Dicksonfjorden, Van Mijenfjorden, and Hornsund fjord is dominantly composed of silicate rocks (e.g., shales, siltstones, sandstones, and metamorphic rocks) (Salvigsen and Høgvard, 2006; Dallmann, 2015) that have abundant radiogenic ^{87}Sr. The fluid that flows through the bedrock could induce the dissolution of silicate minerals and release radiogenic ^{87}Sr to the pore fluids at Sites GC2, GC4, GC6, and GC7.

This mechanism proposed here is different from in situ marine silicate weathering (MSiW), which is coupled to methanogenesis in anoxic sediments (Solomon et al., 2014; Kim et al., 2016; Torres et al., 2020), as our cores did not reach the methanogenesis zone. Such a process increases the $^{87}Sr/^{86}Sr$ values of pore fluids while releasing dissolved cations (e.g., K^+, Mg^{2+}, Ca^{2+}, and Sr^{2+}) and H_4SiO_4 (Wallmann et al., 2008; Solomon et al., 2014; Kim et al., 2016; Hong et al., 2018; Torres et al., 2020), which has not been observed at Sites GC2, GC4, GC6, and GC7 (Figs. 2 and 7). In comparison with pore fluid from Storfjordrenna (offshore Svalbard; maximum $^{87}Sr/^{86}Sr$ = ~0.70987) influenced by the in situ MSiW in anoxic sediment (Hong et al., 2018), the maximum $^{87}Sr/^{86}Sr$ value at Site GC2 is much higher (Fig. 3; Table 3). The analyzed $^{87}Sr/^{86}Sr$ values in the bottom and surface seawater from Site S1 also provide direct evidence for this interpretation. Compared to the present open seawater ($^{87}Sr/^{86}Sr$ value = 0.70917; Paytan et al., 1993) and bottom seawater at Site S8, the $^{87}Sr/^{86}Sr$ value in the surface seawater at Site S1 (water depth = 2.3 mbss) is abnormally high (0.70959) with a much depleted

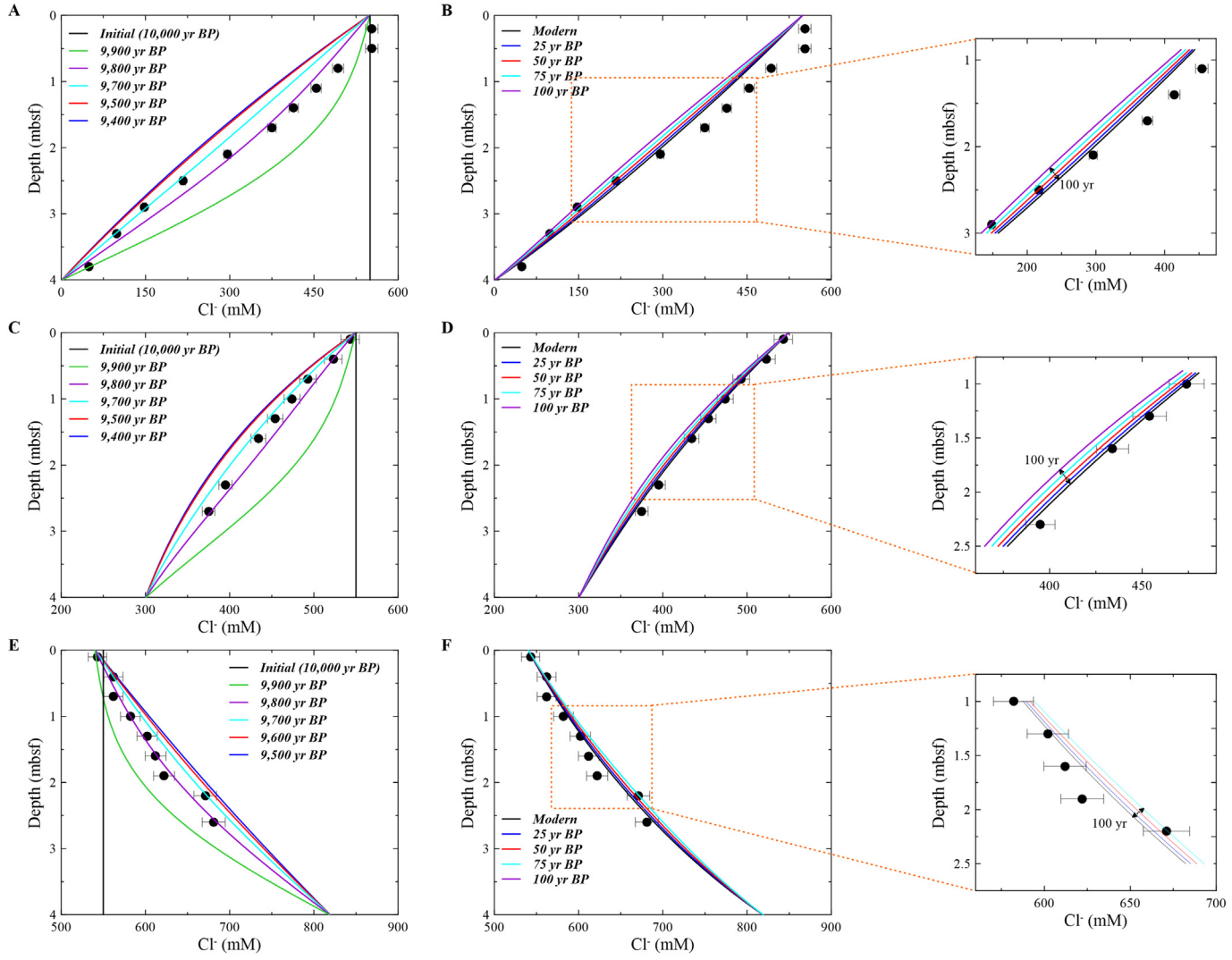

Fig. 6. Time-progressive model results for Sites GC1 (A, B), GC7 (C, D), and GC2 (E, F). Panels A, C, E show the evaluation of downcore dissolved Cl^- profiles for the first five to six hundred years from the initial conditions (10,000 yr BP to 9400 yr BP or 9500 yr BP). A low sedimentation rate (0.05 cm/yr) was assigned to this period. The profiles are then essentially invariable from 9400 yr BP (or 9500 yr BP for Site GC2) until a century ago, when a higher sedimentation rate (0.5 cm/yr) was assigned. In general, it takes ca. 400 (Sites GC1 and GC7) to 500 (Site GC2) years for the pore fluid profiles to evolve from an initial seawater condition to the measured value. The analytical uncertainty of the Cl^- data is <2%.

Cl^- concentration (187 mM), while the bottom seawater at this site (water depth = 36.1 mbss) shows a similar $^{87}Sr/^{86}Sr$ value of 0.70914 with a slightly low Cl^- concentration (523 mM) (Table 2). Since Site S1 is the nearest to the land among the study sites, the impact of terrestrial freshwater with radiogenic ^{87}Sr is greater in the surface seawater by runoff than in the bottom seawater.

Interactions with the Carboniferous to Permian carbonate bedrocks, as documented from Tempelfjorden (Dallmann, 2015), cannot explain the observed radiogenic Sr signals in pore fluids from Site GC1. Given that fluid interacts with the carbonate rocks, the $^{87}Sr/^{86}Sr$ values in pore fluid tend to be similar to those of the carbonate rocks, which reflects the seawater value during its deposition (McArthur et al., 2012). When freshwater migrates from land to the ocean, the $^{87}Sr/^{86}Sr$ value in pore fluids should be similar to that of late Paleozoic seawater if the dissolution of this bedrock has significantly impacted the fluid. However, the reported $^{87}Sr/^{86}Sr$ values in the seawater from the Carboniferous to Permian (~0.7070 to ~0.7085; McArthur et al., 2012) are lower than those of the present seawater and all the pore fluids from Site GC1, which means that the $^{87}Sr/^{86}Sr$ values in pore fluids from this site are not significantly influenced by carbonate bedrock. It is also consistent with our interpretation that the chemical compositions of pore fluids are mainly influenced by water-rock interactions and/or mineral precipitation in contact with silicified carbonate and clastic sedimentary rocks rather than carbonate dissolution at this site. We postulate that the $^{87}Sr/^{86}Sr$ values in pore fluids from Site GC1 reflect mixing with freshwater containing Sr isotope composition similar to that of the present seawater affected by silicate weathering (Fig. 8). Overall, the $^{87}Sr/^{86}Sr$ values in the pore fluids from the Svalbard fjords are mainly controlled by water-rock interactions with the bedrock and/or aquifer of each fjord.

5. Summary and implications

The compositional and isotopic signatures (e.g., depleted Cl^-, $\delta^{18}O$, and δD) of the surface seawater and pore fluids from the studied Svalbard fjords delineate fluid freshening by terrestrial freshwater discharge from precipitation and/or meltwater from the cryosphere (i.e., glacier, permafrost, and snow). The brine pore fluid with low $\delta^{18}O$ and δD values from Site GC2 can be attributed to the rapid formation of submarine permafrost or ice as a result of the readvance of the cryosphere during late Holocene cooling periods. Such a time scale is supported by our numerical simulation, which suggests a time window of ~400 years for brine emplacement. During the formation of such a brine, most dissolved species and light water isotopes

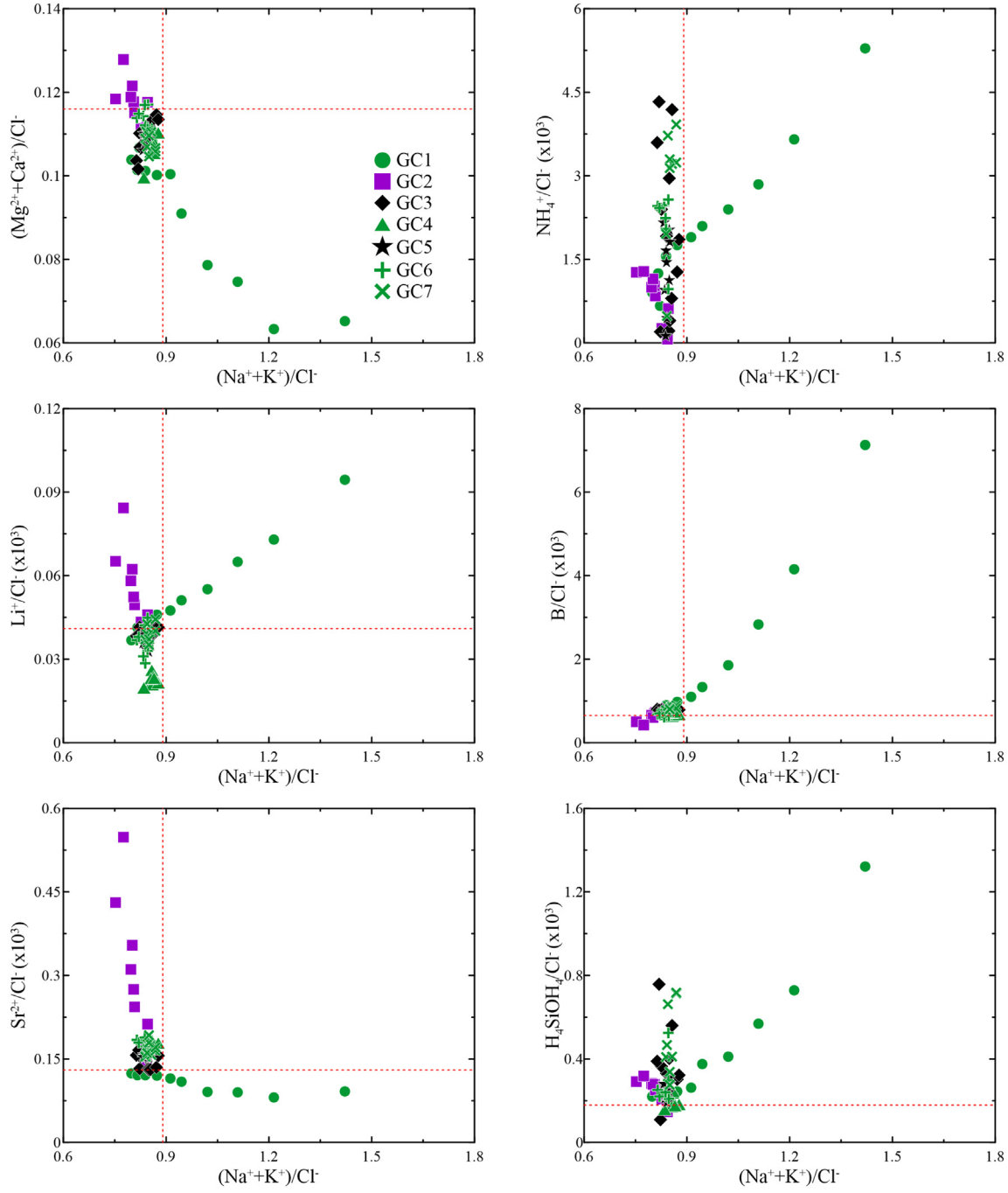

Fig. 7. Scatter plots of $(Mg^{2+} + Ca^{2+})/Cl^-$, NH_4^+/Cl^- (x10³), Li^+/Cl^- (x10³), B/Cl^- (x10³), Sr^{2+}/Cl^- (x10³), and H_4SiO_4/Cl^- (x10³), versus $(Na^+ + K^+)/Cl^-$ in pore fluids from the Svalbard fjords. The read dashed lines show bottom seawater value of Site S8 (water depth = 191.3 mbss).

were excluded from the frozen sediments to the surrounding unfrozen sediments via cryogenic squeezing (Fig. 4A and B).

The pore fluid chemistry shows no clear correlation with water depth and distance from land at each site (Figs. 2 and 3). We propose that the heterogeneity in cryosphere conditions, as well as the subsurface hydrogeology of each fjord, serve as the most important factors determining fluid chemistry. In particular, the cryosphere conditions in each Svalbard fjord have responded differently to Holocene climate change, which has altered the fluid chemistry through interactions between the hydrosphere and cryosphere.

The fluid transported from land to ocean has been modified by multiple water-rock interactions, such as bedrock weathering, (reverse) ion exchanges, and mineral precipitation. In particular, the high $^{87}Sr/^{86}Sr$ values in pore fluids from Sites GC1, GC2, GC4, GC6, and GC7 are strongly controlled by interactions with siliciclastic bedrock and/or aquifers rather than by in situ MSiW (Fig. 4A and B).

The river inputs of dissolved solutes, nutrients (P, N, and Si), and organic matter (dissolved and particulate organic carbon) in association with the shrinkage of the cryosphere extent significantly impact the elemental cycle and biogeochemistry of coastal areas in the Arctic Ocean (Bhatia et al., 2013; Hawkings et al., 2016, 2018; McClelland et al., 2016; Deuerling et al., 2019; Martin et al., 2020). This meltwater transportation will enhance the delivery of these dissolved species in response to future warming. In the Svalbard fjords, we also observe freshwater discharge with enriched $^{87}Sr/^{86}Sr$ and depleted $\delta^{11}B$ and cations in surface seawater and pore fluid (Figs. 2, 3, and 4; Tables 2 and 3). This observation indicates

that significant amounts of these solutes are transported to coastal areas through river runoff and subsurface freshwater flow and impact the water cycle and element budgets of coastal areas in the Svalbard fjords. Additionally, enriched H_4SiO_4 is delivered to the coastal area through subsurface freshwater flow (Figs. 2 and 4; Table 3), which can influence biogeochemical cycles because Si is an essential nutrient for a number of marine organisms (Hawkings et al., 2018). Consequently, our findings suggest that the delivery of dissolved species via subsurface flow is also important for element budgets and biogeochemical cycles in the coastal area of Svalbard and potentially the Arctic Ocean. Future work will need to quantify the out-flow of subsurface freshwater and precisely investigate its impact on the coastal ecosystem compared to surface runoff.

The retreat of the cryosphere has accelerated in the Svalbard fjords during the past several decades in response to rapid global warming (Nuth et al., 2007, 2013; Grabiec et al., 2018), which implies that seawater has rapidly replaced this area and that its influence has gradually increased landward. Indeed the former peninsula in Kongsfjorden is now an island as of the early 1990s and the opening of a strait between Sørkapp Land and the rest of Spitsbergen Island is expected to occur between 2055 and 2065 (Grabiec et al., 2018). These results also suggest that the subsurface fluid in the coastal area may be more salinized landward by natural seawater intrusion as the seawater area expands landward in the Svalbard fjords in association with cryosphere area retreat. It is expected that this retreat will accelerate in the near future (Peterson et al., 2006; Hood et al., 2015), which will expedite natural landward seawater intrusion. Consequently, the present fluid conditions governed by the cryosphere-hydrosphere-lithosphere will undergo remarkable changes. The observed pore fluid compositions at Sites GC1, GC2, and GC3 may serve as an analog for future scenarios. Sites GC1 and GC2 have been directly and strongly influenced by changes in the cryosphere extent during the late Holocene (Joo et al., 2019; Farnsworth et al., 2020), thus pore fluids have been severely affected by fluid freshening or fluid brines in response to varying interactions with the cryosphere (Fig. 4). However, the similarity in fluid composition at Site GC3 to open ocean conditions suggests that the cryosphere-derived influence may diminish depending on the future status of the cryosphere under a future warming scenario (Fig. 4B and C). We predict that the observed unique freshening and brine fluid at Sites GC1 and GC2, respectively, will disappear in the future (Fig. 4C), which will significantly impact the environment from land to the ocean in the Svalbard fjords. Our study emphasizes the need for a better understanding of land-ocean interactions through the subsurface including the role of the cryosphere-hydrosphere-lithosphere and how it influences the element cycles as well as the environment in the Svalbard fjords in response to climate change.

CRediT authorship contribution statement

Ji-Hoon Kim: Conceptualization, Funding acquisition, Project administration, Data curation, Investigation, Writing–original draft, Validation. **Jong-Sik Ryu**: Investigation, Resources, Writing - review & editing. **Wei-Li Hong**: Investigation, Funding acquisition, Validation, Writing - review & editing. **Kwangchul Jang**: Validation, Writing - review & editing, **Young Ji Joo**: Validation, Writing - review & editing. **Damien Lemarchand**: Validation, Resources, Writing - review & editing. **Jin Hur**: Funding acquisition, Writing - review & editing. **Myong-Ho Park**: Writing - review & editing, **Meilian Chen**: Validation, Writing - review & editing.

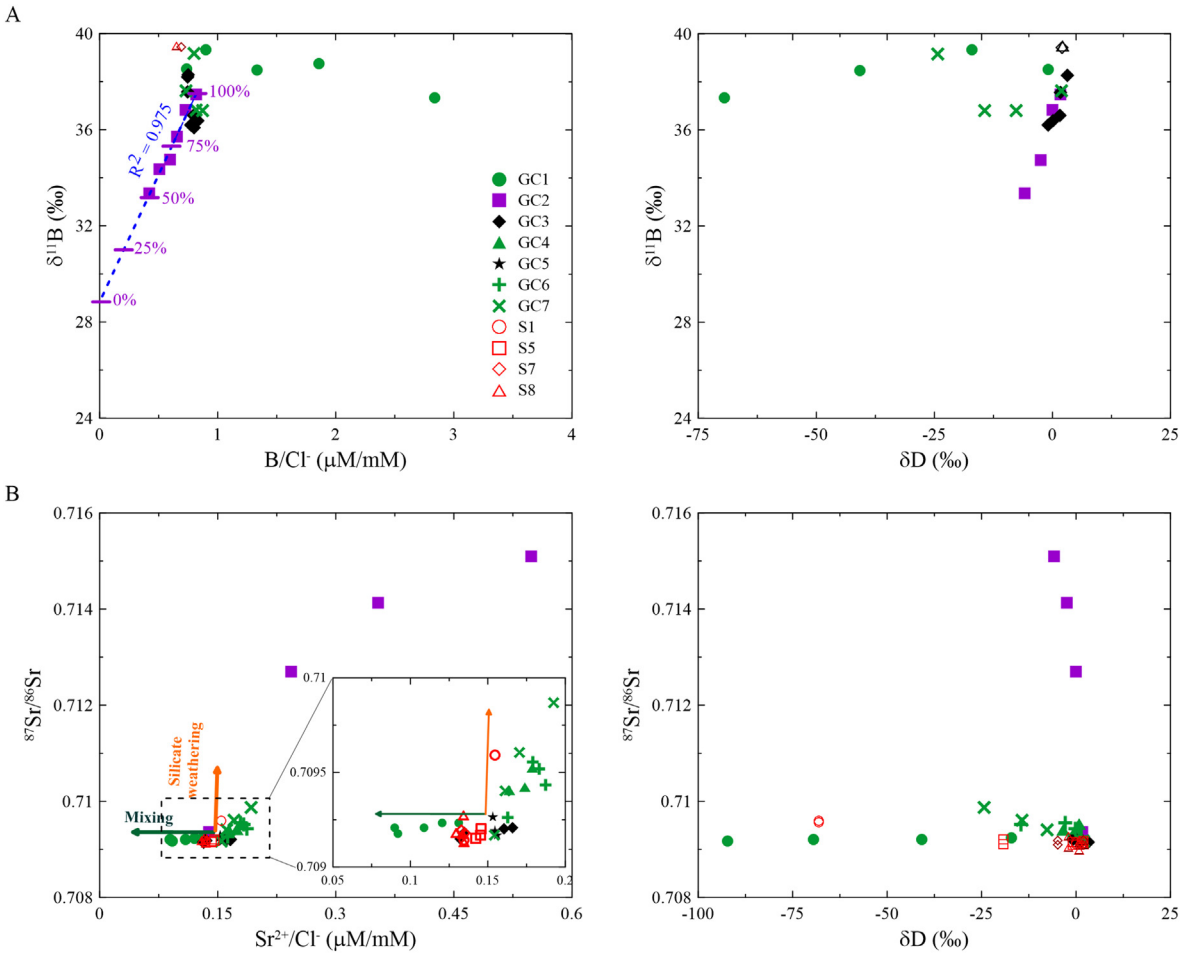

Fig. 8. Scatter plots of (A) $\delta^{11}B$ versus the molar ratio of B/Cl^- ($x10^3$) and δD, and (B) $^{87}Sr/^{86}Sr$ versus the molar ratio of Sr^{2+}/Cl^- ($x10^3$) in seawater and pore fluids from the Svalbard fjords.

Moo-Hee Kang: Investigation, Writing - review & editing. **Sanghee Park**: Resources, Validation, Formal analysis. **Seung-Il Nam**: Validation. **Yun Kyung Lee**: Validation.

Declaration of competing interest

The authors declare that they have no known competing financial interests or personal relationships that could have appeared to influence the work reported in this paper.

Acknowledgment

We would like to thank the shipboard scientific party, captain, and crew of the R/V Helmer Hanssen for the 2016 Expedition. We also gratefully acknowledge the comments from anonymous reviewers, which improved this manuscript. This work was supported by the Korea Ministry of Science and ICT (GP2020-038), the Korea Ministry of Oceans and Fisheries (1525011795), and the Korea Ministry of Trade, Industry and Energy (Project No. 20212010200010). W.-L.H. acknowledges the support from the project ArcticSGD through the Norway Grants and the EEA Grants (UMO-2019/34/H/ST10/00645) and the project, Cyrosphere-driven submarine groundwater in the Arctic, funded by Swedish Research Council (Project No: 2021-04962).

Appendix A. Supplementary data

Supplementary data to this article can be found online at https://doi.org/10.1016/j.scitotenv.2022.155516.

References

Alexeev, S.V., Alexeeva, L.P., 2002. Ground ice in the sedimentary rocks and kimberlites of Yakutia, Russia. Permafr. Periglac. Process. 13, 53–59.
Alexeev, S.V., Alexeeva, L.P., 2003. Hydrogeochemistry of the permafrost zone in the central part of the yakutian diamond-bearing province, Russia. Hydrogeol. J. 1, 574–581.
Appelo, C.A.J., Postma, D., 2005. Geochemistry, Groundwater and Pollution Rotterdam.
Baeten, N.J., Forwick, M., Vogt, C., Vorren, T.O., 2010. Late Weichselian and Holocene sedimentary environments and glacial activity in Billefjorden, Svalbard. Geol. Soc. Spec. Pub. 344, 207–223.
Beszczynska-Möller, A., Węsławski, J.W., Walczowski, W., Zajączkowski, M., 1997. Estimation of glacial meltwater discharge into Svalbard coastal waters. Oceanologia 39, 289–299.
Bhatia, M.P., Das, S.B., Xu, L., Charette, M.A., Wadham, J.L., Kujawinski, E.B., 2013. Organic carbon export from the Greenland ice sheet. Geochim. Cosmochim. Acta 109, 329–344.
Blaszczyk, M., Jania, J.A., Kolondra, L., 2013. Fluctuations of tidewater glaciers in Hornsund Fjord (Southern Svalbard) since the beginning of the 20th century. Polar Res. 34, 327–352.
Charkin, A.N., Rutgers van der Loeff, M., Shakhova, N.E., Gustafsson, Ö., Dudarev, O.V., Cherepnev, M.S., Salyuk, A.N., Koshurnikov, A.V., Spivak, E.A., Gunar, A.Y., Ruban, A.S., Semiletov, I.P., 2017. Discovery and characterization of submarine groundwater discharge in the siberian Arctic seas: a case study in the Buor-Khaya Gulf, Laptev Sea. Cryosphere 11, 2305–2327. https://doi.org/10.5194/tc-11-2305-2017.
Chen, M., Kim, J.-H., Nam, S.-I., Niessen, F., Hong, W.L., Kang, M.-H., Hur, J., 2016. Production of fluorescent dissolved organic matter in Arctic Ocean sediments. Sci. Rep. 6, 39213. https://doi.org/10.1038/srep39213.
Chen, M., Kim, J.-H., Lee, Y.K., Lee, D.-H., Jin, Y.K., Hur, J., 2021. Subsea permafrost as a potential major source of dissolved organic matter to the East Siberian Arctic shelf. Sci. Total Environ. 777, 146100. https://doi.org/10.1016/j.scitotenv.2021.146100.
Christianson, K., Kohler, J., Alley, R.B., Nuth, C., Van Pelt, W.J.J., 2015. Dynamic perennial firn aquifer on an Arctic glacier. Geophys. Res. Lett. 42, 1418–1426. https://doi.org/10.1002/2014GL062806.
Colombo, N., Salerno, F., Gruber, S., Freppaz, M., Williams, M., Fratianni, S., Giardino, M., 2018. Review: impacts of permafrost degradation on inorganic chemistry of surface fresh water. Glob. Planet. Change 162, 69–83. https://doi.org/10.1016/j.gloplacha.2017.11.017.
Dallmann, W.K., 2015. Geoscience Atlas of Svalbard. Norsk Polarinstitutt, Tromsø.
DeFoor, W., Person, M., Larsen, H.C., Lizarralde, D., Cohen, D., Dugan, B., 2011. Ice sheet-derived submarine groundwater discharge on Greenland's continental shelf. Water Resour. Res. 47, W07549. https://doi.org/10.1029/2011WR010536.
Deuerling, K.M., Martin, J.B., Martin, E.E., Abermann, J., Myreng, S.M., Petersen, D., Rennermalm, Å.K., 2019. Chemical weathering across the western foreland of the Greenland ice sheet. Geochim. Cosmochim. Acta 245, 426–440. https://doi.org/10.1016/j.gca.2018.11.025.
Farnsworth, W.R., Allaart, L., Ingólfsson, Ó., Alexanderson, H., Forwick, M., Noormets, R., Retelle, M., Schomacker, A., 2020. Holocene glacial history of Svalbard: status, perspectives and challenges. Earth-Sci. Rev. 208, 103249. https://doi.org/10.1016/j.earscirev.2020.103249.
Forman, S.L., Lubinski, D.J., Ingólfsson, Ó., Zeeberg, J.J., Snyder, J.A., Siegert, M.J., Matishov, G.G., 2004. A review of postglacial emergence on Svalbard, Franz Josef Land and Novaya Zemlya, northern Eurasia. Quat. Sci. Rev. 23, 1391–1434.
Forwick, M., Vorren, T.O., 2009. Late Weichselian and Holocene sedimentary environments and ice rafting in Isfjorden, Spitsbergen. Palaeogeogr. Palaeoclimatol. Palaeoecol. 280, 258–274.
Frankowski, M., Ziola-Frankowska, A., 2014. Analysis of labile form of aluminum and heavy metals in bottom sediments from Kongsfjord, Isfjord, Hornsund fjords. Environ. Earth Sci. 71, 1147–1158.
Frey, K.E., McClelland, J.W., 2009. Impacts of permafrost degradation on arctic river biogeochemistry. Hydrol. Process. 23, 169–182.
Gőrlich, K., 1986. Glacimarine sedimentation of muds in hornsund fjord, Spitsbergen. Ann. Soc. Geol. Pol. 56, 433–477.
Grabiec, M., Ignatiuk, D., Jania, J.A., Moskalik, M., Glowacki, P., Blaszczyk, M., Budzik, T., Walczowski, W., 2018. Coast formation in an Arctic area due to glacier surge and retreat: the Hornbreen-Hambergbreen case from Spistbergen. Earth Surf. Process. Landf. 43, 387–400.
Hagen, J.O., Liestøl, O., Roland, E., Jørgensen, T., 1993. Glacier atlas of Svalbard and Jan Mayen. Norwegian Polar Institute, Norway.
Hagen, J.O., Hohler, J., Melvold, K., Winter, J.-G., 2003. Glaciers in Svalbard: mass balance, runoff and freshwater flux. Polar Res. 22, 145–159.
Hald, M., Dahlgren, T., Olsen, T.E., Lebesbye, E., 2001. Late Holocene palaeoceanography in Van Mijenfjorden, Svalbard. Polar Res. 20, 23–35.
Haldorsen, S., Heim, M., 1999. An arctic groundwater system and its dependence upon climatic change: an example from Svalbard. Permafr. Periglac. Process. 10, 137–149.
Haldorsen, S., Heim, H., Dale, B., Landvik, J.Y., van der Ploeg, M., Leijnse, A., Salvigsen, O., Hagen, J.O., Banks, D., 2010. Sensitivity to long-term climate change of subpermafrost groundwater systems in Svalbard. Quat. Res. 73, 393–402. https://doi.org/10.1016/j.yqres.2009.11.002.
Hanssen-Bauer, I., Førland, E.J., Hisdal, H., Mayer, S., Sandø, A.B., Sorteberg, A., 2019. Climate in Svalbard 2100-A Knowledge Base for Climate Adaptation. Norwegian Centre of Climate Services (NCCS) for Norwegian Environment Agency (Miljødirektoratet), Norway.
Hawkings, J., Wadham, J., Tranter, M., Telling, J., Bagshaw, E., Beaton, A., Simmons, S., Chandler, D., Tedstone, A., Nienow, P., 2016. The Greenland ice sheet as a hot spot of phosphorus weathering and export in the Arctic. Glob. Biogeochem. Cycles 30, 191–210. https://doi.org/10.1002/2015GB005237.
Hawkings, J.R., Hatton, J.E., Hendry, K.R., de Souza, G.F., Wadham, J.L., Ivanovic, R., Kohler, T.J., Stibal, M., Beaton, A., Lamarche-Gagnon, G., Tedston, A., Hain, M.P., Bagshaw, E., Pike, J., Tranter, M., 2018. The silicon cycle impacted by past ice sheets. Nat. Commun. 9, 3210. https://doi.org/10.1038/s41467-018-05689-1.
Hodson, A.J., Nowak, A., Redeker, K.R., Holmlund, E.S., Christiansen, H.H., Turchyn, A.V., 2019. Seasonal dynamics of methane and carbon dioxide evasion from an open system pingo: Lagoon Pingo, Svalbard. Front. Earth Sci. 7, 30. https://doi.org/10.3389/feart.2019.00030.
Hong, W.L., Torres, M.E., Portnov, A., Waage, M., Haley, B., Lepland, A., 2018. Variations in gas and water pulses at an Arctic seep: fluid sources and methane transport. Geophys. Res. Lett. 45, 4153–4162.
Hong, W.L., Lepland, A., Himmler, T., Kim, J.H., Chand, S., Sahy, D., Solomon, E.A., Rae, J.W.B., Martma, T., Nam, S.-I., Knies, J., 2019. Discharge of meteoric water in the eastern Norwegian Sea since the last glacial period. Geophys. Res. Lett. 46, 8194–8204.
Hong, W.L., Lepland, A., Kirsimäe, K., Crémière, A., Rae, J.W., 2022. Boron concentrations and isotopic compositions in methane-derived authigenic carbonates: constraints and limitations in reconstructing formation conditions. Earth Planet. Sci. Lett. 579, 117337. https://doi.org/10.1016/j.epsl.2021.117337.
Hood, E., Battin, T.J., Fellman, J., O'Neel, S., Spencer, R.G.M., 2015. Storage and release of organic carbon from glaciers and ice sheets. Nat. Geosci. 8, 91–96.
Ingólfsson, Ó., Landvik, J.Y., 2013. The Svalbard-Barents Sea ice-sheet – historical, current and future perspectives. Quat. Sci. Rev. 64, 33–60. https://doi.org/10.1016/j.quascirev.2012.11.034.
Jang, K., Bayon, G., Han, Y., Joo, Y.J., Kim, J.H., Ryu, J.S., Woo, J., Forwick, M., Szczucinski, W., Kim, J.H., Nam, S.I., 2020. Neodymium isotope constraints on chemical weathering and past glacial activity in Svalbard. Earth Planet. Sci. Lett. 542, 116319. https://doi.org/10.1016/j.epsl.2020.116319.
Joo, Y.J., Forwick, M., Park, K., Joe, Y.J., Son, Y.J., Nam, S.I., 2019. Holocene environmental changes in Dicksonfjorden, West Spitsbergen, Svalbard. Polar Res. 38, 3426. https://doi.org/10.33265/polar.v38.3426.
Kastner, M., Elderfield, H., Martin, J.B., 1991. Fluids in convergent margins - what do we know about their composition, origin, role in diagenesis and importance for oceanic chemical fluxes. Philos. Trans. R. Soc. A 335, 243–259.
KIGAM, 2016. Preliminary Survey for Marine Energy Resources in the Arctic Region. KIGAM, Daejeon.
Killingtveit, Å., Pettersson, L.-E., Sand, K., 2003. Water balance investigations in Svalbard. Polar Res. 22, 161–174.
Kim, J.-H., Torres, M.E., Hong, W.-L., Choi, J., Riedel, M., Bahk, J.-J., Kim, S.H., 2013. Pore fluid chemistry from the second gas hydrate drilling expedition in the Ulleung Basin (UBGH2): source, mechanisms and consequences of fluid freshening in the central part of the Ulleung Basin, East Sea. Mar. Petrol. Geol. 47, 99–112.
Kim, J.-H., Torres, M.E., Haley, B.A., Ryu, J.S., Park, M.H., Hong, W.-L., Choi, J., 2016. Marine silicate weathering in the anoxic sediment of the Ulleung Basin: evidence and consequences. Geochem.Geophys. Geosyst. 17, 3437–3453.
Kim, J.-H., Hong, W.-L., Torres, M.E., Ryu, J.-S., Kang, M.-H., Han, D., Nam, S.-I., Hur, J., Koh, D.-C., Niessen, F., Lee, D.-H., Jang, K., Rae, J.W.B., Chen, M., 2021. A pulse of meteoric subsurface fluid discharging into the Chukchi Sea during the Early Holocene Thermal

Maximum (EHTM). Geochem. Geophys. Geosyst. 22, e2021GC009750. https://doi.org/10.1029/2021GC009750.
Kowalski, P.M., Wunder, B., 2018. Boron isotope fractionation among vapor-liquids-solids-melts: experiments and atomistic modeling. In: Marschall, H., Foster, G. (Eds.), Boron Isotopes: The Fifth Element (Advances in Isotope Geochemistry). Springer International Publishing, Cham, pp. 33–69.
Lecher, A.L., Kessler, J., Sparrow, K., Garcia-Tigreros Kodovska, F., Dimova, N., Murray, J., Tulaczyk, S., Paytan, A., 2016. Methane transport through submarine groundwater discharge to the North Pacific and Arctic Ocean at two Alaskan sites. Limnol. Oceanogr. 61, S344–S355. https://doi.org/10.1002/lno.10118.
Levitan, M.A., Levchenko, O.V., Murdmaa, I.O., Peresypkin, V.I., Roshchina, I.A., Tolmacheva, A.V., 2008. History of sedimentation in Isfjord (Western Spitsbergen). Lithol. Miner. Resour. 43, 520–541.
Loeng, H., 1991. Features of the physical oceanographic conditions of the Barents Sea. Polar Res. 10, 5–18.
Mangerud, J., Svendsen, J.I., 2018. The Holocene Thermal Maximum around Svalbard, Arctic North Atlantic; molluscs show early and exceptional warmth. Holocene 28, 65–83. https://doi.org/10.1177/0959683617715701.
Martin, J.B., Pain, A.J., Martin, E.E., Rahman, S., Ackerman, P., 2020. Comparisons of nutrients exported from Greenlandic glacial and deglaciated watersheds. Glob. Biogeochem. Cycles 34, e2020GB006661. https://doi.org/10.1029/2020GB006661.
McArthur, J.M., Howarth, R.J., Shields, G.A., 2012. Strontium Isotope Stratigraphy. In: Gradstein, F.M., Ogg, J.G., Schmotz, M.D., Ogg, G.M. (Eds.), The Geologic Time Scale 2012. vol. 1. Elsevier Science, pp. 127–144.
McClelland, J.W., Holmes, R.M., Peterson, B.J., Raymond, P.A., Striegl, R.G., Zhulidov, A.V., Zimov, S.A., Zimov, N., Tank, S.E., Spencer, R.G.M., Staples, R., Gurtovaya, T.Y., Griffin, C.G., 2016. Particulate organic carbon and nitrogen export from major Arctic rivers. Glob. Biogeochem. Cycles 30, 629–643. https://doi.org/10.1002/2015GB005351.
Meier, K.-D., Thannheiser, D., 2009. Gletscher und permafrost in Nordenskiøldland Spitzbergen, als potentielle Klimaindikatoren. University of Hamburg, Hamburg.
Micallef, A., Person, M., Haroon, A., Weymer, B.A., Jegen, M., Schwalenberg, K., Faghih, Z., Duan, S., Cohen, D., Mountjoy, J.J., Woelz, S., 2020. 3D characterisation and quantification of an offshore freshened groundwater system in the Canterbury Bight. Nat. Commun. 11, 1372. https://doi.org/10.1038/s41467-020-14770-7.
Muckenhuber, S., Nilsen, F., Korosov, A., Sandven, S., 2016. Sea ice cover in Isfjorden and Hornsund, Svalbard (2000–2014) from remote sensing data. Cryosphere 10, 149–158.
Nuth, C., Kohler, J., Aas, H.F., Brandt, O., Hagen, J.O., 2007. Glacier geometry and elevation changes on Svalbard (1936–90): a baseline dataset. Ann. Glaciol. 46, 106–116.
Nuth, C., Moholdt, G., Kohler, J., Hagen, J.O., Kääb, A., 2010. Svalbard glacier elevation changes and contribution to sea level rise. J. Geophys. Res. 115, F01008. https://doi.org/10.1029/2008JF001223.
Nuth, C., Kohler, J., Konig, M., von Deschwanden, A., Hagen, J.O., Kääb, A., Moholdt, G., Pettersson, R., 2013. Decadal changes from a multi-temporal glacier inventory of Svalbard. Cryosphere 7, 1603–1621.
Olichwer, T., Tarka, R., Modelska, M., 2012. Chemical composition of groundwaters in the Hornsund region, southern Spitsbergen. Hydrol. Res. 44, 117–130. https://doi.org/10.2166/nh.2012.075.
Onarheim, I.H., Smedsrud, L.H., Ingvaldsen, R.B., Nilsen, F., 2014. Loss of sea ice during winter north of Svalbard. Tellus A: Dyn. Meteorol. Oceanogr. 66, 23933. https://doi.org/10.3402/tellusa.v66.23933.
Paytan, A., Kastner, M., Martin, E.E., Macdougall, J.D., Herbert, T., 1993. Marine barite as a monitor of seawater strontium isotope composition. Nature 366, 445–449.
Peeters, B., Pedersen, Å.Ø., Loe, L.E., Isaksen, K., Veiberg, V., Stien, A., Kohler, J., Gallet, J.-C., Aanes, R., Hansen, B.B., 2019. Spatiotemporal patterns of rain-on-snow and basal ice in high Arctic Svalbard: detection of a climate-cryosphere regime shift. Environ. Res. Lett. 14, 015002. https://doi.org/10.1088/1748-9326/aaefb3.
Peral, M., Austin, W.E.N., Noormets, R., 2022. Identification of Atlantic water inflow on the North Svalbard shelf during the Holocene. J. Quat. Sci. 37, 86–99. https://doi.org/10.1002/jqs.3374.
Peterson, B.J., Holmes, R.M., McClelland, J.W., Vorosmarty, C.J., Lammers, R.B., Shiklomanov, A.I., Shiklomanov, I.A., Rahmstorf, S., 2002. Increasing river discharge to the Arctic Ocean. Science 298, 2171–2173.
Peterson, B.J., McClelland, J., Curry, R., Holmes, R.M., Walsh, J.E., Aagaard, K., 2006. Trajectory shifts in the Arctic and subarctic freshwater cycle. Science 313, 1061–1066.
Plassen, L., Vorren, T.O., Forwick, M., 2004. Integrated acoustic and coring investigation of glacigenic deposits in Spitsbergen fjords. Polar Res. 23, 89–110.
Polyakov, I.V., Walsh, J.E., Kwok, R., 2012. Recent changes of Arctic multiyear sea ice coverage and the likely causes. Bull. Am. Meteorol. Soc. 93, 145–151.
Rasmussen, T.L., Thomsen, E., 2014. Palaeoceanographic development in Storfjorden, Svalbard, during the deglaciation and Holocene: evidence from benthic foraminiferal records. Boreas 44, 24–44. https://doi.org/10.1111/bor.12098.
Roux, P., Lemarchand, D., Hughes, H.J., Turpault, M.P., 2015. A rapid method for determining boron concentration (ID-ICP-MS) and delta B-11 (MC-ICP-MS) in vegetation samples after microwave digestion and cation exchange chemical purification. Geostand. Geoanal. Res. 39, 453–466.
Salvigsen, O., Høgvard, K., 2006. Glacial history, Holocene shoreline displacement and palaeoclimate based on radiocarbon ages in the area of Bockfjorden, North-Western Spitsbergen, Svalbard. Polar Res. 25, 15–24.
Sauer, S., Hong, W.-H., Yao, A., Lepland, M., Klug, M., Eichinger, F., Himmler, T., Crémière, A., Panieri, G., Schubert, C.J., Knies, J., 2021. Methane transport and sources in an Arctic deep-water cold seep offshore NW Svalbard (Vestnesa Ridge, 79°N). Deep-Sea Res. Part I Oceanogr. Res. Pap. 167, 103430. https://doi.org/10.1016/j.dsr.2020.103430.
Semiletov, I.N., Shakhova, V., Romanovsky, 2004. Methane climate forcing and methane observations in the Siberian Arctic land-shelf system. World Resou. Rev. 16, 503–514.
Serreze, M.C., Stroeve, J., Barrett, A.P., Boisvert, L.N., 2016. Summer atmospheric circulation anomalies over the Arctic Ocean and their influences on September Sea ice extent: a cautionary tale. J. Geophy. Res. Atmos. 121, 11463–11485. https://doi.org/10.1002/2016JD025161.
Shouakar-Stash, O., Alexeev, S.V., Frape, S.K., Alexeeva, L.P., Drimmie, R.J., 2007. Geochemistry and stable isotopic signatures, including chlorine and bromine isotopes, of the deep groundwaters of the Siberian Platform, Russia. Appl. Geochem. 22, 589–605.
Solomon, E.A., Spivack, A.J., Kastner, M., Torres, M.E., Robertson, G., 2014. Gas hydrate distribution and carbon sequestration through coupled microbial methanogenesis and silicate weathering in the Krishna-Godavari Basin, offshore India. Mar. Petrol. Geol. 58, 233–253.
Stotler, R.L., Frape, S.K., Ruskeeniemi, T., Ahonen, L., Onstott, T.C., Hobbs, M.Y., 2009. Hydrogeochemistry of groundwaters in and below the base of thick permafrost at Lupin, Nunavut, Canada. J. Hydrol. 373, 80–95.
Svendsen, J.I., Mangerud, J., 1997. Holocene glacial and climatic variations on Spitsbergen, Svalbard. The Holocene 7, 45–57.
Svendsen, J.I., Elverhmi, A., Mamgerud, J., 1996. The retreat of the Barents Sea Ice Sheet on the western Svalbard margin. Boreas 25, 244–256.
Teichert, B.M.A., Torres, M.E., Bohrmann, G., Eisenhauer, A., 2005. Fluid sources, fluid pathways and diagenetic reactions across an accretionary prism revealed by Sr and B geochemistry. Earth Planet. Sci. Lett. 239, 106–121.
Torres, M.E., Wallmann, K., Trehu, A.M., Bohrmann, G., Borowski, W.S., Tomaru, H., 2004. Gas hydrate growth, methane transport, and chloride enrichment at the southern summit of Hydrate Ridge, Cascadia margin off Oregon. Earth Planet. Sci. Lett. 226, 225–241.
Torres, M.E., Hong, W.L., Solomon, E.A., Milliken, K., Kim, J.H., Sample, J.C., Teichert, B.M.A., Wallmann, K., 2020. Silicate weathering in anoxic marine sediment as a requirement for authigenic carbonate burial. Earth-Sci. Rev. 200, 102960. https://doi.org/10.1016/j.earscirev.2019.102960.
van der Bilt, W.G.M., D'Andrea, W.J., Bakke, J., Balascio, N.L., Werner, J.P., Gjerde, M., Bradley, R.S., 2018. Alkenone-based reconstructions reveal four-phase Holocene temperature evolution for High Arctic Svalbard. Quat. Sci. Rev. 183, 204–213. https://doi.org/10.1016/j.quascirev.2016.10.006.
Van Pelt, W.J.J., Pohjola, V., Pettersson, R., Marchenko, S., Kohler, J., Luks, B., Hagen, J.O., Schuler, T.V., Dunse, T., Noël, B., Reijme, C., 2019. A long-term dataset of climatic mass balance, snow conditions, and runoff in Svalbard (1957–2018). Cryosphere 13, 2259–2280. https://doi.org/10.5194/tc13-2259-2019.
Vikhamar-Schuler, D., Isaksen, K., Haugen, J.E., Tommervik, H., Luks, B., Schuler, T.V., Bjerke, J.W., 2016. Changes in winter warming events in the Nordic Arctic Region. J. Clim. 29, 6223–6244.
Wallmann, K., Aloisi, G., Haeckel, M., Tishchenko, P., Pavlova, G., Greinert, J., Kutterolf, S., Eisenhauer, A., 2008. Silicate weathering in anoxic marine sediments. Geochim. Cosmochim. Acta 72, 2895–2918.
Werner, A., 1993. Holocene moraine chronology, Spitsbergen, Svalbard: lichenometric evidence for multiple Neoglacial advances in the Arctic. The Holocene 3, 128–137.
Yoon, H.I., Kim, Y., Yoo, G.-C., Lee, J.I., Nam, S.-I., 2006. Holocene glaciomarine sedimentation and its paleoclimatic implication on the Svalbard Fjord in the Arctic Sea. Ocean Polar Res. 28, 1–12.
Yoshikawa, K., Harada, K., 1995. Observations on nearshore pingo growth, Adventdalen, Spitsbergen. Permafr. Periglac. Process. 6, 361–372.